

Kent Academic Repository

Full text document (pdf)

Citation for published version

Samal, M.R. and Chen, W.P. and Takami, M. and Jose, J. and Froebrich, Dirk (2018) YSO jets in the Galactic Plane from UWISH2: V - Jets and Outflows in M17. *Monthly Notices of the Royal Astronomical Society*, 477 (4). pp. 4577-4595. ISSN 0035-8711.

DOI

<https://doi.org/10.1093/mnras/sty853>

Link to record in KAR

<http://kar.kent.ac.uk/66603/>

Document Version

Author's Accepted Manuscript

Copyright & reuse

Content in the Kent Academic Repository is made available for research purposes. Unless otherwise stated all content is protected by copyright and in the absence of an open licence (eg Creative Commons), permissions for further reuse of content should be sought from the publisher, author or other copyright holder.

Versions of research

The version in the Kent Academic Repository may differ from the final published version.

Users are advised to check <http://kar.kent.ac.uk> for the status of the paper. **Users should always cite the published version of record.**

Enquiries

For any further enquiries regarding the licence status of this document, please contact:

researchsupport@kent.ac.uk

If you believe this document infringes copyright then please contact the KAR admin team with the take-down information provided at <http://kar.kent.ac.uk/contact.html>

YSO jets in the Galactic Plane from UWISH2: V - Jets and Outflows in M17

M. R. Samal^{1*}, W. P. Chen¹, M. Takami², J. Jose^{3,4}, D. Froebrich⁵

¹*Graduate Institute of Astronomy, National Central University 300, Jhongli City, Taoyuan County - 32001, Taiwan*

²*Institute of Astronomy and Astrophysics, Academia Sinica, PO Box 23-141, Taipei 10617, Taiwan*

³*Indian Institute of Science Education and Research, Rami Reddy Nagar, Karakambadi Road, Mangalam (P.O.) Tirupati 517507, India*

⁴*Kavli Institute for Astronomy and Astrophysics, Peking University, Yi He Yuan Lu 5, Haidian Qu, Beijing 100871, China*

⁵*Centre for Astrophysics & Planetary Science, The University of Kent, Canterbury, Kent CT2 7NH, UK*

ABSTRACT

Jets and outflows are the first signposts of stellar birth. Emission in the H₂ 1-0 S(1) line at 2.122 μm is a powerful tracer of shock excitation in these objects. Here we present the analysis of 2.0 × 0.8 deg² data from the UK Widefield Infrared Survey for H₂ (UWISH2) in the 1-0 S(1) line to identify and characterize the outflows of the M17 complex. We uncover 48 probable outflows, of which, 93 per cent are new discoveries. We identified driving source candidates for 60 per cent of the outflows. Among the driving source candidate YSOs: 90 per cent are protostars and the remainder 10 per cent are Class II YSOs. Comparing with results from other surveys, we suggest that H₂ emission fades very quickly as the objects evolve from protostars to pre-main-sequence stars. We fit SED models to 14 candidate outflow driving sources and conclude that the outflows of our sample are mostly driven by moderate-mass YSOs that are still actively accreting from their protoplanetary disc. We examined the spatial distribution of the outflows with the gas and dust distribution of the complex, and observed that the filamentary dark-cloud “M17SWex” located at the south-western side of the complex, is associated with a greater number of outflows. We find our results corroborate previous suggestions, that in the M17 complex, M17SWex is the most active site of star formation. Several of our newly identified outflow candidates are excellent targets for follow up studies to better understand very early phase of protostellar evolution.

2 *Samal et al.*

Key words: stars: formation, ISM: individual objects: Galactic Plane, ISM: jets and outflows, ISM: H II region, infrared: stars.

1 INTRODUCTION

Jets and outflows are common signatures of stellar birth. They are thought to represent two aspects of the same mass-loss phenomenon responsible for removal of angular momentum from the star-disc system, allowing accretion to proceed and the star to grow. Observationally, a strong correlation between mass accretion and mass-loss has been observed in young stars (e.g. [Hartmann et al. 1998](#)), favoring the fact that outflows indeed play a significant role in the growth and evolution of young stars. In this context, while much has been learned about the evolved class II-III phases of pre-main sequence (PMS) stars from observations and modeling (e.g. [Cabrit 2007](#)), the evolution of class 0/I objects, where the roles of the outflows are significant and stars get most of their mass, is less understood. Similarly, another important related question concerning outflows is the driving mechanisms. Models fall broadly into two categories of: from the interface between the star’s magnetosphere and disc, i.e. the “X-wind model” and from a wide range of disc radii, i.e. the “disk-wind model” (details can be found in [Ray 2007](#)). Understanding which one of the two models is dominant, requires investigation of a large sample of outflow bearing young stars, as outflows show a wide variety of morphologies (e.g. [Arce et al. 2007](#), and references therein). Therefore, detecting and characterizing outflows from the youngest protostellar sources holds the key towards the understanding of the evolution of protostars as well as their launching mechanisms.

In this context, near-infrared emission at $2.12 \mu\text{m}$ ($\text{H}_2 \nu = 1-0 \text{ S}(1)$) is one of the ideal tools to search for shock-excited outflows in terms of jets and knots from young sources. This line is an excellent tracer of hot ($T \sim 2000 \text{ K}$) and dense ($n \geq 10^3 \text{ cm}^{-3}$) gas excited by the fast shocks ($10\text{--}100 \text{ km s}^{-1}$) caused by the interactions of jets with the surrounding interstellar medium (e.g. [Stanke et al. 2002](#)). Moreover, for large-scale studies, outflow morphologies with near-infrared observations are more successful in identifying the outflow driving sources (particularly in the crowded region) compared to the molecular observations that typically lack the spatial resolution and depth to identify the fainter outflows. Jets are believed to be the highly compressed ejecta of the accelerated entrained gas of the ambient medium. The jets and winds drive slower moving molecular lobes called bipolar molecular outflows.

* E-mail:manash.samal3@gmail.com

Although many studies using H_2 observations have focused on identification and characterization of outflow sources in nearby clouds (e.g. [Hodapp 2007](#); [Davis et al. 2007, 2009](#); [Kumar et al. 2011](#); [Khanzadyan et al. 2012](#); [Bally et al. 2014](#); [Zhang et al. 2015](#)), searches for outflow sources on galactic scales are still lacking. In the last decade, a few hundreds individual young stellar objects (YSOs) with outflows, i.e. so-called “Extended Green Objects (EGOs)”, have been identified in the Galactic plane using the *Spitzer* 4.5 μm band observations (e.g. [Cyganowski et al. 2008, 2009](#)) of the GLIMPSE survey. GLIMPSE is, however, a shallow survey—the faintest EGOs identified in GLIMPSE survey have surface brightnesses in 4.5 μm images $\geq 4 \text{ MJy sr}^{-1}$. In comparison, the majority of the diffuse green emission in NGC1333 (distance $\sim 250 \text{ pc}$) has 4.5 μm surface brightness $\leq 4 \text{ MJy sr}^{-1}$ ([Gutermuth et al. 2008](#)). Thus GLIMPSE survey is more sensitive to massive young stellar objects (MYSOs) outflows in distant star-forming regions.

The advanced wide field sensitive infrared telescopes in recent years have enabled the explorations of outflow candidates in the infrared waveband over galactic scales. In this regard, the UKIRT Widefield Infrared Survey for H_2 (UWISH2; [Froebrich et al. 2011](#)) conducted with United Kingdom Infrared Telescope (UKIRT) at 2.12 μm ($H_2 \nu = 1-0 \text{ S}(1)$) has opened a new avenue to search for outflows from the YSOs (e.g. [Ioannidis & Froebrich 2012a,b](#); [Froebrich & Makin 2016](#); [Makin & Froebrich 2018](#)), even possibly from low-mass YSOs (e.g. [Ioannidis & Froebrich 2012b](#)). We note the surface brightness limit of the UWISH2 survey in the H_2 narrow-band filter is 300-2000 times better than the H_2 emission strength of the GLIMPSE survey at 4.5 μm band ([Froebrich et al. 2011](#)), thus in general a likely better tracer of outflows, however, we emphasize that in the region of high extinction the visibility of H_2 emission can be poor compared to 4.5 μm emission. Moreover, in the context of protostar detection, in recent years, the instruments of the *Spitzer* Space Telescope and the *Herschel* Space Observatory have improved the resolution and sensitivity in the mid- and far-infrared domain where protostars emit the bulk of their energy. In fact, many well-known class 0/I protostars have been detected between 3.6 and 8 μm with rising spectral energy distributions (SEDs) between 24 to 70 μm (e.g. [Enoch et al. 2009](#); [Manoj et al. 2013](#); [Dunham et al. 2015](#)). So combining *Spitzer* and *Herschel* data with the 2.12 μm observations, it is now possible to identify deeply embedded outflow bearing class 0/I protostars in a star-forming complex that are too faint or extinguished to be detected with the previous shorter-wavelength facilities (e.g. 2MASS, UKIDSS, GLIMPSE surveys).

In this work, we make use of UWISH2, *Spitzer* and *Herschel* data to identify and characterize the outflow driving young protostars of the M17 cloud complex, which is at a moderate distance and currently producing young stars at a high-rate. This work is organized as follows: Section 2

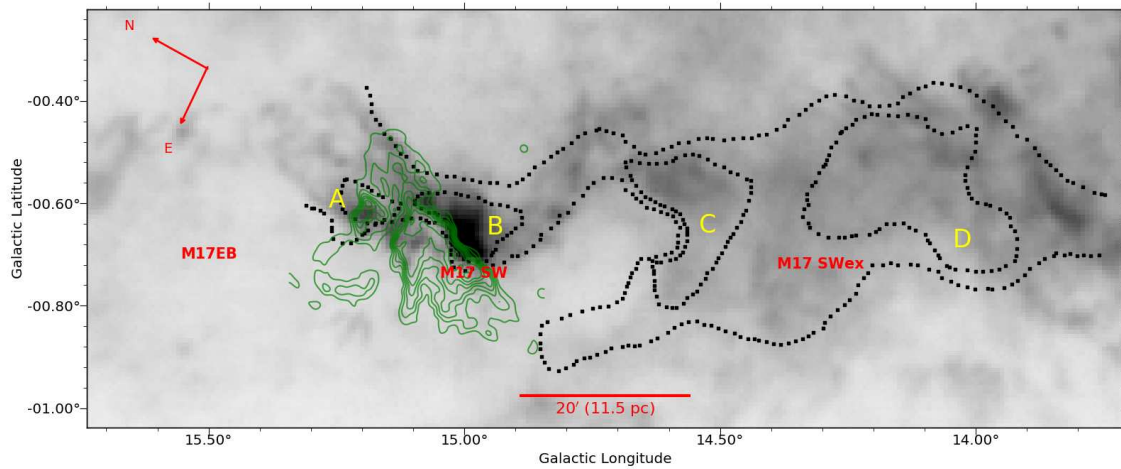
4 *Samal et al.*

Figure 1. ^{12}CO map (grey-scale) of the M17 complex showing the distribution of molecular gas. The map is obtained at a resolution of ~ 46 arcsec with the Purple Mountain Observatory (PMO) 13.7-m telescope (Jiang et al. in preparation). The green contours correspond to the VLA 20 cm (at 0.05, 0.14, 0.24, 0.34, 0.43, 0.53, 0.63, 0.73, 0.83 and 0.93 Jy/Beam; resolution ~ 6 arcsec) emission from Helfand et al. (2006), while the black contours represent the ^{13}CO emission (at 5 K and 10 K; resolution ~ 2.3 arcmin) from Elmegreen et al. (1979). The field size is $\sim 2.0 \times 0.8$ deg 2 (or 70×28 pc 2). The four dense fragments which has been designated by the letters A (in the NE) through D (in the extreme SW) are also marked.

describes the M17 complex. Section 3 discusses the various data sets and photometric catalogues. In Section 4, we discuss the identification of outflows and outflow driving candidate YSOs, and physical properties of the candidate YSOs by fitting the YSO models to their observed SEDs. Section 5 discusses the general nature of outflows, comparison with other similar surveys and also presents a few interesting cases. Section 6 describes the star formation scenario of M17 with the aid of spatial distribution and correlation of the identified outflows with the gas and dust of the complex. Section 7 summarizes the various results obtained.

2 THE M17 COMPLEX

M17 ($l \sim 15^\circ.09$, $b \sim -00^\circ.75$), located at the north-east edge of one of the largest giant molecular clouds (size ~ 70 pc \times 15 pc and mass $\geq 2 \times 10^5 M_\odot$; Elmegreen et al. (1979)) in the Sagittarius-Carina arm of our Galaxy, is a blister H II region (also known as Omega Nebula, W38, S45), and is the second brightest thermal radio source in the sky after Orion. It is illuminated by the massive, 1–3 Myr old (Jiang et al. 2002) stellar cluster NGC 6618, whose earliest O stars are an O4-O4 binary called ‘Kleinmann’s Anonymous Star’.

The giant molecular cloud (GMC) as observed in the low-resolution (~ 2.3 arcmin) ^{13}CO , contains four major fragments, namely A, B, C and D, each of mass $\geq 4 \times 10^4 M_\odot$ (Elmegreen et al. 1979). The local standard of rest velocity (V_{LSR}) and line width of these components are in the range of 20–22 km s $^{-1}$ and 3.8–5.1 km s $^{-1}$, respectively. From the velocity structure of the ^{12}CO and ^{13}CO gas, Elmegreen et al. (1979) suggests that most of the CO emission of the GMC

comes from a single cloud of velocity around 20 km s^{-1} although the cloud has fragmented and there is a gradual change in velocity structure in the complex from northeast to southwest. The peak velocity increases from $20 \pm 1 \text{ km s}^{-1}$ in the northeast to about $22 \pm 1 \text{ km s}^{-1}$ to the extreme southwest. They argued that these differences in velocity pattern may be related to the recent passage of a spiral density wave, which would have moved from northeast to southwest in this part of the Galaxy.

Figure 1 shows the overview of the complex, with all the above components marked. It also shows the distribution of ionized gas associated with the H II region. Among the fragments, the high-excitation temperature and compact fragments, A and B, are located in the northeast side of the complex very close to the H II region, whereas the low-excitation temperature and larger fragments, C and D, are located farther away from the H II region in its south-western direction. Among the fragments, the fragments B usually referred to as M17 SW (Thronson & Lada 1983; Guesten & Fiebig 1988), while after the discovery of flying dragon like dark cloud by *Spitzer* in the extended region of M17 SW (i.e. in the D component of the GMC), the D component is usually known as M17 SWex (Povich & Whitney 2010; Povich et al. 2013). The infra-red dark cloud (IRDC), G14.225-0.506, comprises the central region of M17 SWex, where dense filamentary ammonia gas (at $V_{\text{LSR}} \sim 20 \text{ km s}^{-1}$) and hub systems have been observed (Busquet et al. 2013). Besides, Povich et al. (2007), from the CO observations, detected a coherent shell-like structure in the eastern side of the H II region with local standard of rest velocity ($V_{\text{LSR}} \sim 19 \text{ km s}^{-1}$). The shell is coincident with the bubble walls of a cavity observed in the *Spitzer* images (Fig. 1). Povich et al. (2007), named it as the M17 extended bubble (M17 EB).

The V_{LSR} and FWHM line width of the ionized gas associated to the H II region is 18.6 km s^{-1} and 3.2 km s^{-1} , respectively (Joncas & Roy 1986). Since the velocity of the various dense components (Elmegreen et al. 1979; Busquet et al. 2013) are similar to the ionized gas velocity of M17, the bright H II region and the dense fragments are part of the same cloud. The spectrophotometric distance for NGC 6618 is estimated to be in the range 2.1–2.2 kpc (Chini et al. 1980; Hoffmeister et al. 2008), consistent with the kinematic distance $\sim 2.2 \text{ kpc}$ obtained from the radial velocity measurements of the ionized gas (Georgelin et al. 1973; Joncas & Roy 1986). Along the same line, using trigonometric parallax of CH_3OH masers ($V_{\text{LSR}} \sim 23 \pm 3 \text{ km s}^{-1}$), the recent VLBI observations have estimated a distance $1.98^{+0.14}_{-0.12} \text{ kpc}$ (Wu et al. 2014) to M17, which we have adopted in this work.

Star formation towards M17 has been extensively studied by Povich et al. (2007), Povich & Whitney (2010) and Povich et al. (2016). Their results suggest that M17 is currently producing

6 *Samal et al.*

stars at a rate $\geq 0.005 M_{\odot} \text{ yr}^{-1}$, \sim four times the star formation rate of the Orion Nebula Cluster (see [Povich et al. 2016](#)). Thus a potential site where one would expect a large number of protostars. In the present work, we focus our study on an area $\sim 2.0 \times 0.8 \text{ deg}^2$ of the complex, primarily covering the dense clouds and the extended bubble.

3 OBSERVATIONS AND DATA SETS

We retrieved the narrow-band continuum subtracted $\text{H}_2 \nu = 1-0 \text{ S}(1) 2.12 \mu\text{m}$ images from the UWISH2 database¹ ([Froebrich et al. 2011](#)). UWISH2 is an unbiased survey of the inner Galactic plane in the H_2 line at $2.12 \mu\text{m}$, using the WFCAM camera at UKIRT. The survey covers $\sim 209 \text{ deg}^2$ along the inner Galactic Plane from $l \approx 357^\circ$ to $l \approx 65^\circ$ and $|b| \leq 1^\circ.5$. WFCAM houses four Rockwell Hawaii-II (HgCdTe 2048×2048) arrays spaced by 94 per cent in the focal plane. For UWISH2 observations, 12 exposures were acquired at each telescope pointing, resulting in a total exposure time per pixel of 720 s. The typical full width half-maximum (FWHM) of the stellar point spread function (PSF) of the UWISH2 observations is 0.7 arcsec, and the typical 5σ detection limit of point sources is ~ 18 magnitude and the surface brightness limit is $\sim 4.1 \times 10^{-19} \text{ W m}^{-2}$. In order to perform the continuum subtraction of the narrow band images UWISH2 uses the UKIDSS data in the K-band ($2.2 \mu\text{m}$) taken with the same telescope and instrumental set-up as part of Galactic Plane Survey (GPS; [Lucas et al. 2008](#)). The GPS survey maps 1800 square degrees of the galactic plane ($|b| < 5^\circ$) in the J, H and K bandpasses with total exposure time per pixel of 80, 80 and 40 s, respectively, reaching 5σ detection limit of J ~ 19.8 , H ~ 19.0 , and K ~ 18.0 magnitude, respectively. The typical FWHM of the GPS survey is 0.9 arcsec. We used the continuum subtracted H_2 images to identify jets and knots in the M17 complex.

The M17 complex was observed by the *Spitzer* Space Telescope as part of the Galactic Legacy Infrared Mid-Plane Survey Extraordinaire (GLIMPSE; [Benjamin et al. 2003](#)) and the Multiband Imaging Photometer GALactic plane survey (MIPSGAL; [Carey et al. 2009](#)). We obtained the Post Basic Calibrated Data (PBCD) images of the *Spitzer* Infrared Array Camera (IRAC) at 3.6, 4.5, 5.8 and $8.0 \mu\text{m}$, and of the Multiband Imaging Photometer (MIPS) at $24.0 \mu\text{m}$ from the *Spitzer* Archive² to search for embedded YSOs and to examine the morphology of the inter-stellar medium (ISM) at the location of jets and knots. For point sources, we used the UKDISS *JHK* ([Lucas et al. 2008](#)), GLIMPSE IRAC ([Carey et al. 2009](#)) and MIPSGAL $24 \mu\text{m}$ ([Gutermuth &](#)

¹ <http://astro.kent.ac.uk/uwish2/>

² <http://sha.ipac.caltech.edu/applications/Spitzer/SHA/>

Heyer 2015) point source catalogues available on the VizieR³ interface. Note that, the 3.6 and 4.5 μm bands are more sensitive to stellar photospheres than the 5.8, 8.0 and 24 μm bands, and the angular resolution of the images at IRAC bands is in the range 1.7–2.0 arcsec, whereas at MIPS 24 μm band it is ~ 6.0 arcsec.

For this work, we also downloaded the 70 μm images from the *Herschel* Science Archive⁴, observed as part of the Hi-GAL survey (Molinari et al. 2010), using the Photodetector Array Camera and Spectrometer (PACS). The angular resolution of the Hi-GAL data at 70 μm is ~ 10 arcsec. To get point source fluxes, we performed photometry on the *Herschel* 70 μm image using the IRAF tasks *daofind* and *apphot* to extract the positions of the sources and to perform aperture photometry. We used an aperture radius of 12 arcsec, and inner and outer sky annulus of 35 and 45 arcsec, respectively, and applied the aperture correction as documented by the PACS team (Balog et al. 2014). Since our target sources are embedded in strongly varied spatial structures, the variations in the background limit the photometric accuracy. We thus used different apertures and estimated that our photometry is accurate within 10 to 15 per cent.

The above point source catalogues are used to identify the YSOs in the vicinity of the jets/knots and construct their SEDs. Note that the MIPS GAL 24 μm catalogue comes along with its GLIMPSE-IRAC counterparts. For making various color-color or color-magnitude plots between 3.6 to 70 μm (in search for YSOs close to the knots and jets), we matched astrometric position of the MIPS GAL 24 μm catalogue with the astrometric position of the 70 μm sources using a position-matching tolerance of 6 arcsec⁵ (the FWHM of the 24 μm data). For making the SED of the selected YSOs, we visually inspected the images and catalogues of the YSOs using *Aladin* software, then matched the already made 3.6 to 70 μm catalogue to the UKDISS catalogue using a matching radius of 2 arcsec (the FWHM of the GLIMPSE data) to obtain data points between 1.2 to 70 μm . In a few cases, where there were more than one source within the matching radius, we considered the closest one as the best match.

In addition, we also exploit information from the following major available surveys in search for early stages of star formation such as cold cores/clumps or SiO emission, in the vicinity of the jets/knots:

- (i) We used Csengeri et al. (2014) catalogue of compact objects from the APEX Telescope

³ <http://vizier.u-strasbg.fr/viz-bin/VizieR-4>

⁴ <http://archives.esac.esa.int/hsa/whsa/>

⁵ We note the astrometric accuracy of the MIPS GAL images is better than 1 arcsec, while it is less than 2 arcsec for the Hi-Gal images

8 *Samal et al.*

Large Area Survey of the Galaxy (ATLASGAL) survey at $870\ \mu\text{m}$ (beam ~ 19.2 arcsec, sensitivity $\sim 50\text{--}70$ mJy/beam) for identifying clumps/cores.

(ii) We used [Rosolowsky et al. \(2010\)](#) catalogue of compact objects from the Bolocam Galactic Plane Survey (BGPS; [Aguirre et al. 2011](#)) at $1.1\ \text{mm}$ (beam ~ 33 arcsec, sensitivity $\sim 30\text{--}60$ mJy/beam) for identifying clumps/cores.

(iii) [Reid & Wilson \(2006\)](#) used the Submillimeter Common-User Bolometer Array (SCUBA) on the James Clerk Maxwell Telescope (beam ~ 15.4 arcsec, sensitivity ~ 27 mJy/beam) to map an approximately $12\ \text{arcmin} \times 12\ \text{arcmin}$ region around the M17 H II region at $850\ \mu\text{m}$. We used their catalogue for our analysis.

(iv) SiO emission is a strong signpost of outflows from the very youngest, class 0/I, sources (e.g. [Gibb et al. 2004](#); [Codella et al. 2007](#); [Tafalla et al. 2015](#)), although other explanations are possible, such as low-velocity shocks caused by large-scale flow collisions during global collapse or by the dynamical interaction of two clouds (e.g. see [López-Sepulcre et al. 2016](#), and references therein). Recently [Csengeri et al. \(2016\)](#) conducted a survey on massive clumps with the IRAM 30-m and APEX telescopes at the frequency of the SiO (2-1) and (5-4) transitions. In the present work, we used the catalogue of [Csengeri et al. \(2016\)](#) in search of SiO emission at the location of the MHOs, although this sample is only for clumps of mass greater than $650\ M_{\odot}$. Note that the spatial position of the shock-excited SiO and $2.12\ \mu\text{m}$ emission for a given outflow can be different as they are sensitive to different physical conditions.

We note, owing to the different resolutions of the above mm-submm surveys, when we have multiple spatial positions for a given clump we considered the spatial position of the highest resolution as the better representation of its true position. We also note that the association of individual clumps/cores of the above surveys with the M17 complex required velocity information. However, it is worth mentioning that there are mainly two cloud components in the direction of M17 (particularly in the direction of C and D components), at $V_{\text{LSR}} \sim 20$ and 40 ([Lada 1976](#)); and as seen by ^{13}CO , the emission from the latter component is mainly distributed in the latitude range -0.2° to 0.00° (e.g. [Umemoto et al. 2017](#)), therefore unrelated to the area studied in this work. Moreover, from the work of [Busquet et al. \(2013\)](#) one can find that the most dense dust continuum clumps of M17SWex are positionally coinciding with the velocity of the ammonia gas at $V_{\text{LSR}} \sim 20 \pm 2\ \text{km s}^{-1}$. Since dense gas is more related to star formation, we thus assume that contamination of other line of sight galactic dust clumps should be less in our studied area.

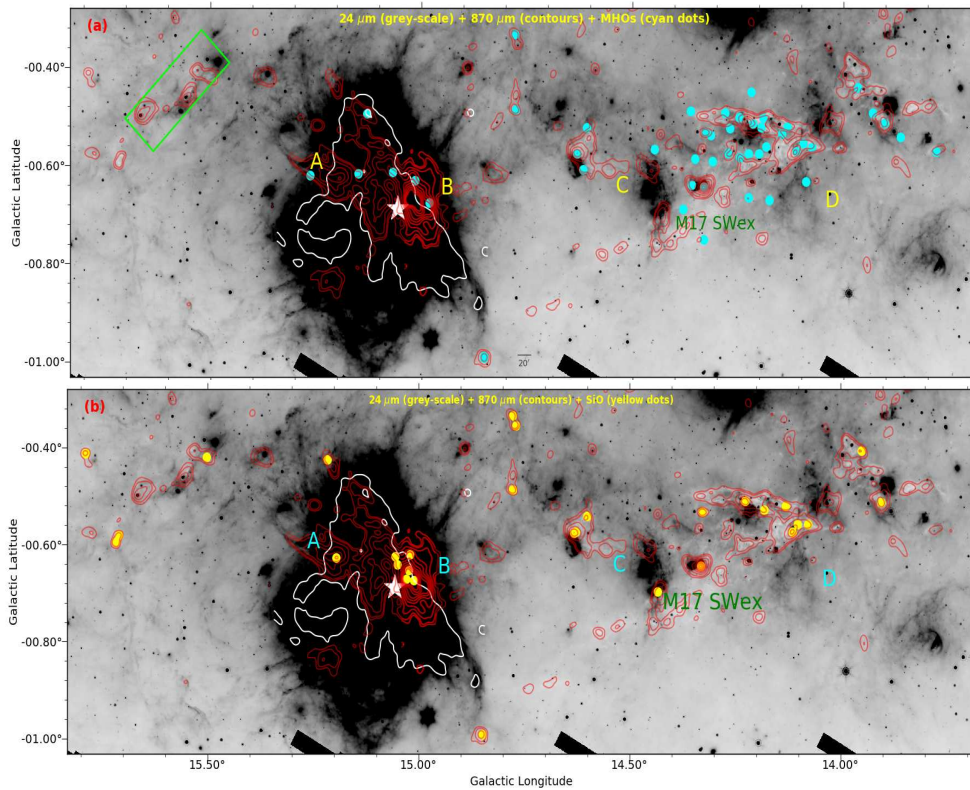


Figure 2. Figure showing the distributions of MHO based outflows (top-panel) and SiO emissions (bottom-panel) in the M17 complex on the 24 μm background image. Red contours represent the 870 μm dust continuum emission from the ATLASGAL survey. Contour levels are at geometric progression in square root two, starting at 0.1 Jy/beam and ending at 7.5 Jy/beam. The outer extent of the main H II region is shown in white contour (~ 0.05 Jy/beam at 21 cm). The star symbol denotes the central location of the cluster NGC 6618. The green rectangle represents the area of the complex that is not covered by UWISH2; it lies at the edges of UWISH2 tiles.

4 RESULTS

4.1 Identification of the outflows and outflow driving sources

Our first goal is to identify the shocked H_2 features. To do so, we searched for jets or knots or bow-shock features in the continuum subtracted ($\text{H}_2 - \text{K}$) images. These sources tend to show up as enhanced emission over the background $\text{H}_2 - \text{K}$ image. However, identifying the true shock-excited features in the $\text{H}_2 - \text{K}$ images is not straight forward, as they can be confused with several other artifacts. These include but are not limited to: (i) the fluorescence excited features by the UV field from a nearby massive star; (ii) the artifacts present in the residual images due to improper continuum subtraction; (iii) artifacts due to the sources of high proper motion or with excess emission.

One potential way to avoid such artifacts is to look at the multiwavelength data corresponding to the H_2 features. We therefore, checked the morphology and strength of the emissions at 1.2, 2.2, 4.5, and 8 μm images corresponding to each H_2 emission. Artifacts due to improper continuum subtraction or proper motion or artifacts of the bright stars can be identified using 2.2

Table 1. Properties of the MHOs

ID	MHO number ¹	Lon. ² (degree)	Lat. ² (degree)	Length ³ (pc)	Source Type. ⁴	Luminosity ⁵ (L_{\odot})	Comments
01	MHO 2308	13.78040	-0.57323	0.22	class O/I	27	bipolar, two opposite symmetric streamers
02	MHO 2309	13.86546	-0.54239	–	–	–	three interconnected compact knots
03	MHO 2310	13.90317	-0.51448	–	cluster	–	group of compact knots
04	MHO 2311	13.93151	-0.49345	–	–	–	an isolated bright compact knot
05	MHO 2312	13.96643	-0.44227	–	–	–	two compact knots
06	MHO 2313	14.07504	-0.56333	0.20	class O/I	27	monopolar, an elongated patchy emission
07	MHO 2314	14.08924	-0.63322	–	–	–	an isolated compact knot with some diffuse nebulosity
08	MHO 2315	14.09521	-0.63386	–	–	–	an elongated knotty structure
09	MHO 2316	14.11298	-0.57489	–	cluster	–	a patch of diffuse emission
10	MHO 2317	14.13259	-0.52206	0.45	class O/I	252	bipolar, a jet-shaped structure and two compact knots
11	MHO 2318	14.14622	-0.53602	–	–	–	an isolated compact knot
12	MHO 2319	14.17600	-0.67032	–	–	–	two aligned knot-like structures
13	MHO 2320	14.17929	-0.56165	–	class II	–	monopolar, a patch of elongated faint emission
14	MHO 2321	14.19136	-0.50404	–	cluster	13	bipolar, chain of compact knots
15	MHO 2322	14.19463	-0.52274	0.22	class I/O	53	monopolar, two compact knots
16	MHO 2323	14.20004	-0.57689	–	–	–	two faint interconnected knots
17	MHO 2324	14.21574	-0.51510	0.82	class O/I	–	bipolar, three compact jet-like structures along a line
18	MHO 2325	14.21841	-0.45140	–	–	–	a bright head-tail like structure
19	MHO 2326	14.22462	-0.66556	0.09	class O/I	34	monopolar, an elongated head-tail like structure
20	MHO 2327	14.22495	-0.57625	–	–	–	three bright knots connected with some diffuse emission
21	MHO 2328	14.24515	-0.58420	0.30	class O/I	22*	bipolar, two opposite asymmetric jets
22	MHO 2329	14.24661	-0.50227	0.30	class O/I	53*	monopolar, a jet-like structure
23	MHO 2330	14.27437	-0.53161	–	–	–	two compact knots
24	MHO 2331	14.27447	-0.57511	0.78	class O/I	19*	bipolar, chain of elongated faint emission
25	MHO 2332	14.28056	-0.49345	–	–	–	a bright compact knot
26	MHO 2333	14.31092	-0.59261	0.73	class II	286	bipolar, chain of knots, bend morphology
27	MHO 2334	14.31447	-0.53895	–	–	–	chain of elongated faint emission
28	MHO 2335	14.32700	-0.53257	0.55	core	–	monopolar, an elongated faint emission
29	MHO 2336	14.33115	-0.75052	–	–	–	two bow-shock shaped structures
30	MHO 2306	14.33145	-0.64355	0.45	class O/I	4827*	bipolar, two bright elongated knots
31	MHO 2337	14.35227	-0.58742	0.07	class O/I	4*	bipolar, two opposite symmetric jets
32	MHO 2338	14.36143	-0.63861	0.41	core	–	monopolar, a compact knot with a faint streamer
33	MHO 2339	14.36161	-0.48936	–	–	–	a bright knot with some patchy emission
34	MHO 2340	14.38114	-0.68939	–	–	–	elongated faint diffuse emission
35	MHO 2341	14.44860	-0.56711	0.38	core	–	bipolar, two opposite streamer-like structures
36	MHO 2342	14.60962	-0.52421	–	–	–	a faint elongated head-tail like structure
37	MHO 2343	14.61739	-0.60949	0.28	class O/I	–	bipolar, compact knots with some patchy emission
38	MHO 2344	14.63169	-0.57720	0.43	class O/I	715	monopolar, multiple elongated knots
39	MHO 2345	14.77681	-0.48768	0.56	class O/I	147	bipolar, chain of patchy knots along a line
40	MHO 2346	14.77861	-0.33277	0.19	class O/I	827	monopolar, an elongated continuous flow
41	MHO 2307	14.85161	-0.99178	0.19	class O/I	92	bipolar, compact bright knots
42	MHO 2347	14.85168	-0.98854	1.2	class O/I	70	bipolar, chain of knots
43	MHO 2348	14.98216	-0.67674	0.68	cluster	–	monopolar, a bow-shaped structure with a faint tail
44	MHO 2349	15.01505	-0.63124	–	–	–	a compact bright knot with a diffuse tail
45	MHO 2350	15.06827	-0.61351	0.21	core	–	bipolar, two faint lobe-like structures
46	MHO 2351	15.12872	-0.49566	0.19	class O/I	20	bipolar, three compact knots
47	MHO 2352	15.14967	-0.61683	0.24	core	–	bipolar, two opposite bright lobes
48	MHO 2353	15.25981	-0.61653	0.6	core	–	monopolar, two faint knots near to a core

¹ The MHO numbers are assigned in the order of their right ascensions. Prior to this work, the MHOs 2306 and 2307 have been identified by [Lee et al. \(2012\)](#) and [Caratti o Garatti et al. \(2015\)](#), respectively. Thus they are appearing in the middle of the table according to their right ascensions.

² The coordinates are: (i) coordinates of the driving source if one found; (ii) coordinates of the peak intensity if the MHO constitutes an isolated knot; (iii) central coordinates of the knots if the MHO constitutes multiple knots without a driving source candidate.

³ Only for objects with a driving source we measured the apparent length. Quoted lengths are end-to-end for bipolar outflows or twice of the source-to-end for monopolar flows.

⁴ We note, evolution of massive protostars differ significantly from the evolution of low-mass protostars (e.g. [Hosokawa & Omukai 2009](#)), however, unlike the case of low-mass stars there is no observational evolutionary sequence that is firmly established for high-mass stars, thus in this work we have tentatively adopted the classification of the low-mass stars for the high-mass stars.

⁵ Luminosities are either from SED models or using only $70 \mu\text{m}$ flux. Estimates based on the later method are marked with asterisks. These luminosities are accurate within a factor of two.

μm images (e.g. see discussion in [Ioannidis & Froebrich 2012a](#)). Similarly, fluorescence excited H_2 features can be picked up using near-infrared colour-composite images and/or *Spitzer* 8 μm images. Because fluorescence excited features appear brownish in the JKH_2 RGB images as the J - and K -band continuum filters contain additional excited emission-lines (e.g. [Makin & Froebrich 2018](#)). Similarly, 8 μm IRAC band contains the 7.7 and 8.8 μm emission features commonly attributed to polycyclic aromatic hydrocarbons (PAH) molecules ([Reach et al. 2006](#)), and can be excited in the photo-dissociation-regions (PDRs) of a cloud by the absorption of UV photons from nearby massive stars (e.g. [Povich et al. 2007](#)). Thus, the close resemblance of diffuse H_2 and 8 μm emission at the peripheries of the H II regions or structures pointing toward the massive stars, are more likely representation of the UV fluorescence excitation. In contrast to 8 μm , the 4.5 μm band contains both H_2 and CO lines, that can become bright in the presence of shocked molecular gas, such as those expected from protostellar outflows (e.g. see discussion in [Noriega-Crespo et al. 2004](#); [Takami et al. 2010, 2011](#)). Hence, enhanced diffuse emission at 4.5 μm at the location of H_2 emission features, is a supportive indication of the presence of shocked outflow, although part of the 4.5 μm emission can be scattered continuum light from the embedded YSOs ([Takami et al. 2012](#)). In the literature, outflows identified based on the enhanced extended 4.5 μm emission are referred as “EGOs” (e.g. [Cyganowski et al. 2008](#)) or “Green Fuzzies” (e.g. [De Buizer & Vacca 2010](#)), and are generally identified by making IRAC colour composite images (using 8.0, 4.5 and 3.6 μm bands as red, green and blue colours, respectively) as the 4.5 μm emission stands out against other IRAC band emissions. In this work, we have also used the *Spitzer* 4.5 μm and 8.0 μm band as a tool by making IRAC colour-composite images to search for extra outflow components (if any) in the vicinity of 2.12 μm features (particularly in the highly extinguished regions of a cloud such as dense clumps, as the extinction effect at 4.5 μm band is nearly half of that of the K -band) or to trace the PDRs around the massive stars.

We also looked at the morphology of the H_2 features to disentangle possible Planetary nebula (e.g. see discussion in [Ramos-Larios et al. 2017](#)) from the wide-angle outflows.

Admittedly, the above criteria of identifying H_2 features are somewhat subjective, and the possibility of missing faint and small H_2 emission features exists. None the less, comparing the number shocked H_2 features identified by us with the automatically generated shocked H_2 catalogue of the UWISH2 survey ([Froebrich et al. 2015](#)), we find that both the catalogues are in good agreement with each other. For example, both the catalogues have 93 per cent common sources. This ensures that the identified H_2 features are highly reliable and affirmed that the false-positive rate in the UWISH2 catalogue, if at all present, is likely to be less than 7 per cent.

12 *Samal et al.*

The acronym ‘MHO’ stands for molecular hydrogen emission-line object associated with the jets and outflows (Davis et al. 2010). Several clusters of H₂ shock features in the region can be clearly associated with coherent outflow, we therefore followed the procedure outlined in Davis et al. (2010), i.e. when it is possible to correlate multiple knots or jets to a single outflow, we assigned them as a single MHO, otherwise, we considered each discrete jet or knot as an MHO. Briefly, we inspected large-scale H₂ images in the search for possible large-scale flows. On the large-scale images, we looked for possible bow-shock features or aligned jets/knots. We then extended a line tracing the middle of the bow-shocks or knot/jets in search for possible counter bow-shocks or jets/knots in the opposite symmetric axis. For only a few cases, we observed a chain of jets/knots over parsec-scale dimensions, but the majority of the jets/knots are found to be isolated or confined to only small spatial scale. We then based on the appearance/shape of the emission features, and the alignment of features with each other and/or the potential driving sources, we assigned an MHO number to a jet/knot or a chain of jets/knots or a group of jets/knots (explained in more detail below). With the above approach, we identified 48 likely outflows within our surveyed area. We list their positions in Table 1, while their distribution in the complex, and correlation with cold gas at 870 μm and shocked SiO emission are shown in Fig. 2. We discuss the general star-formation of the complex with the aid of these distributions in Section 6. We note, as grouping weak emission features into an outflow is a complex problem, thus in this work, we treat each identified outflow (particularly those without a driving source) as a candidate, pending verification through other shock tracers (e.g. Plunkett et al. 2013; Zinchenko et al. 2015), though most them will very likely turn into true outflows.

Here we describe our methodology of identifying YSOs and cores, and connecting them to the jets/knots. The details concerning the classification of potential point sources into various YSO classes are given in Appendix A. In summary, keeping in mind that the visibility of a point source at any given band is a strong function of the evolutionary status of the source itself, the extinction around its vicinity, and sensitivity of that particular band, we used several flux ratios between 3.6 to 70 μm to classify all those potential sources that are in the close vicinity of jets/knots into different YSO classes (for details see Section A). When possible we also used the available YSO catalogues from the literature. After identifying YSOs in the vicinity of jets/knots, we noticed that several jets/knots are not associated with any YSO candidates, which led us to think that these jets/knots are possibly originating from molecular cores in their earliest evolutionary phases such as from first hydro- static cores (e.g. Pezzuto et al. 2012; Gerin et al. 2015) or 70 μm dark cores (e.g. Feng et al. 2016; Aso et al. 2017). It is also quite possible that: i) these jets/knots are

part of large flows from distant sources; ii) the driving sources are still embedded in dense cores and are too faint to be detected in the *Spitzer* and *Herschel* bands (see Section 5.1 for further discussion). To account for the sources that are either in the earliest evolutionary phases or deeply embedded in dense cores, we searched for early stages of star formation such as cold cores/clumps or infrared dark cloud fragments or SiO emission (see Section 3) in the vicinity of the jets/knots. After identifying YSOs and cores, in the next step we tried to connect them with the nearby jets/knots. Briefly, as the outflow symmetries can be different types, for example, as described in Bally (2007), S- and Z-shaped symmetries can occur if the outflow axis changes over time due to precession induced by a companion or interactions with sibling stars in a cluster, while C-shaped bend of outflow axis can occur due to the motion of surrounding gas or the motion of the outflow source itself, so identifying potential outflow driving sources is not trivial in the cases of misaligned outflows. Therefore, while connecting YSOs/cores with the jets/knots, we considered all those sources whose positions are compatible with the various jet shapes such as straight-, curved-, or S-shaped. Along with the evolutionary status of the YSOs, we also used the indicators such as extended $4.5\ \mu\text{m}$ and/or shock tracer SiO emission to approve or reject, whether or not any given source or core is responsible for the jets/knots observed in its vicinity. In a few rare cases, where we have two closeby sources, we gave higher priority to the younger and luminous YSOs, as luminous YSOs drive stronger outflows (e.g. Caratti o Garatti et al. 2015; Manoj et al. 2016).

Here we describe two complicated examples of our approach on the connection of the potential driving sources (cores or YSOs) with the jets/knots. Figure 3 illustrates an example of our approach on the search for potential driving sources around jets/knots. As can be seen, this region consists of two elongated H_2 jets. Together they appear to form an east-west flow. Three potential sources, visible in different bands between 3.6 to $70\ \mu\text{m}$ (marked as 21a, 21b and 21c, in the figure), lies in the vicinity of the jets. Among the sources, the source 21a lies at the centre of jets and is visible in all the IRAC bands, the source 21b lies at one end of the MHO and is only visible in the $70\ \mu\text{m}$, while the source 21c lies slightly away from the flow axis, and is only visible at 4.5 and $24\ \mu\text{m}$. Either of them can be the outflow driving source, although the possibility of 21c is less as it is not along the flow axis. The evolutionary status of the sources 21a and 21b are identified, respectively, in the Figs. A2 and A2c of Appendix A. In short, the source 21a is not a YSO as its location coincides with the the zone of the field stars in the $[5.8]$ versus $[5.8] - [8.0]$ diagram, it has no emission at $24/70\ \mu\text{m}$ and in the literature it is not an infrared excess YSO (e.g. Povich & Whitney 2010). On the other hand, the source 21b has the characteristics of an early class 0 source and it is bright in $70\ \mu\text{m}$. Although the location of 21b is somewhat intriguing, but it could be due to

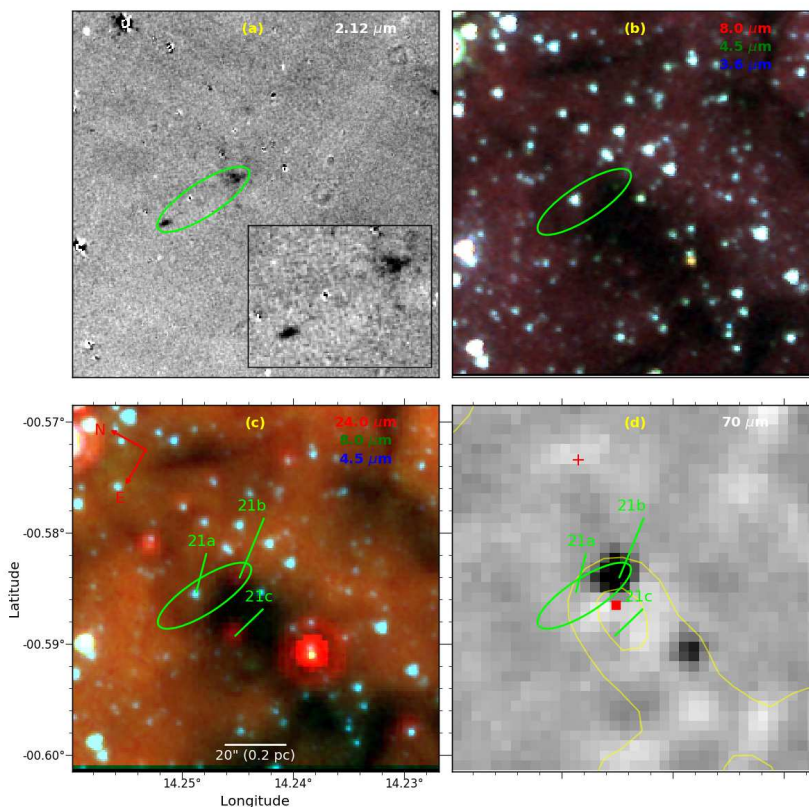
14 *Samal et al.*

Figure 3. An example figure showing multiwavelength view of ISM around an MHO. (a) The continuum subtracted H_2 image, revealing the H_2 jets. The inset figure shows the zoomed view of the jets. (b) *Spitzer*-IRAC colour-composite image ($3.6 \mu\text{m}$ in blue, $4.5 \mu\text{m}$ in green and $8.0 \mu\text{m}$ in red); used to search for enhanced $4.5 \mu\text{m}$ emission such as those found in EGOs. (c) *Spitzer*-IRAC/MIPS composite-colour image ($4.5 \mu\text{m}$ in blue, $8 \mu\text{m}$ in green and $24 \mu\text{m}$ in red); used to unveil deeply embedded protostars. (d) The grey-scale unsharp masked $70 \mu\text{m}$ image; used in search for early class 0 sources such as PACS Bright Red sources (see Section A). Green contours show the distribution of $870 \mu\text{m}$ emission (from the ATLASGAL survey). The position of the outflow on the *Spitzer* and $70 \mu\text{m}$ images is shown with an ellipse and the major axis of the ellipse indicates the likely flow direction.

projection effect or anisotropy of the medium. It is worth mentioning, [Froeblich & Makin \(2016\)](#), in their study of the Cassiopeia and Auriga complex, found that ~ 20 per cent of the bipolar flows are asymmetric in nature with length ratio < 0.5 . Since there are no other potential sources along the presumed flow axis of the jets (marked with an ellipse), thus 21b is the very likely driving source of the jets. Figure 4 depicts another example where three H_2 jet-like features along with all the aforementioned signposts of star-formation, including an EGO, have been found. As can be seen, the jet-like features lie at the eastern outskirts of an ATLASGAL clump (shown in contours) and a bright $24 \mu\text{m}$ source (marked as ID 38) lies at the centre of the clump. One can see the middle jet connects well to the point source through the enhanced diffuse $4.5 \mu\text{m}$ emission. The clump is also at the location of SiO emissions. The column density in the direction of the clump is of the order of $\sim 10^{23} \text{ cm}^{-2}$ (e.g. [Csengeri et al. 2016](#)), perhaps the possible reason why we do not see H_2 emission in the vicinity of the source. Deep high-resolution molecular observations would be needed to track the origin of these infrared jet-like structures (e.g. [Plunkett et al. 2013](#); [Zinchenko et al. 2018](#)). None the less, it is worth mentioning, multiple wide-angle H_2 bullets and

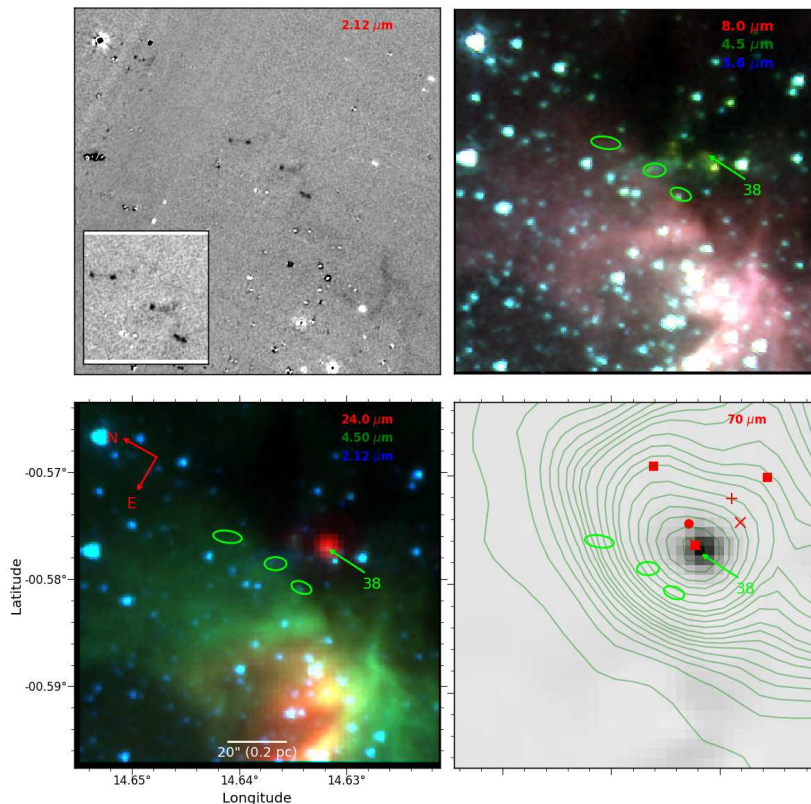


Figure 4. An example figure showing signs of star formation such as extended green emission, SiO maser (\times), cold clumps from the ATLASGAL (\blacksquare) and BGPS (\bullet) surveys and IRDC fragments ($+$) at the location of an outflow consisting of three jet-like structures (rounded by oval shaped marks). In this work, we have considered that the jets are part of a single outflow whose origin lies in the clump (see text for details). All the images have the same meaning as in Fig. 3.

jet-like structures have been reported for a few cases (e.g. Sahai et al. 2008; Bally et al. 2011). The nature of such explosive outflows is still not well understood but it is believed that it might be related to dynamical decay of non-hierarchical system of stars or protostellar merger or close passage of two protostars (e.g. see discussion in Bally et al. 2015, 2017; Sahai et al. 2017). In the present work, we tentatively consider that all the three jet-like features are part of a single outflow and are likely driven by the point source(s) embedded in the clump. The source 38 being luminous and class-0 type, could be the dominant source responsible for the flow.

Figures 3 and 4 are the illustration for two outflows. We followed a similar prescription for all the MHOs. The detailed discussion on the individual MHOs is given in Appendix B, where we present multiwavelength large-scale ($\sim 1 \times 1 \text{ pc}^2$ area) images around the MHOs, provide notes on individual objects and discuss their driving sources. Briefly, following the above approach, we associate 26 YSOs/cores and 4 clusters (i.e. the driving source is situated in a group of stars and we could not single it out) with the 48 MHO features. The spectral nature of the driving sources are also tabulated in Table 1. Out of 26 YSOs/cores, 6 are cores without point sources up to $70 \mu\text{m}$, 18 are protostars (class 0/I YSOs) and 2 are evolved sources (class II YSOs).

16 *Samal et al.*

4.2 Physical properties of the driving sources

4.2.1 SED modeling of the YSOs

To get deep insight into the nature of the YSOs identified in the present work, we modeled the observed SEDs using the models of [Robitaille et al. \(2006, 2007\)](#). The models used a Monte-Carlo based radiation transfer code of [Whitney et al. \(2003a,b\)](#) to follow photons emitted by the central star as they are scattered, absorbed and re-emitted throughout the disk and envelope system. The code uses a number of combinations of central star, disc, in-falling envelope and bipolar cavity, for a reasonably large parameter space. While other techniques (e.g. colour-colour diagrams or spectral indices) can be useful in identifying the evolutionary class, the SED models have the ability to infer physical information about the young stars such as total luminosity, stellar age and mass and accretion rates, accounting the geometry of the disc and envelope. However, interpreting SEDs using radiative transfer codes is subject to degeneracies, which spatially-resolved multiwavelength observations can overcome (e.g. see [Samal et al. 2015](#)). Thus, we fit SED models to only those candidate YSOs for which we have constraints on the $70 \mu\text{m}$ flux along with the fluxes at shorter wavebands between 1.2 to $24 \mu\text{m}$.

For the SED fitting, we adopted a distance 2 ± 0.2 kpc and a visual extinction (A_V) range 2 to 50 magnitude with lower-limit corresponds to the foreground extinction to M17 (e.g. [Hoffmeister et al. 2008](#)), while the upper-limit in line with typical maximum values found towards EGOs (e.g. [Caratti o Garatti et al. 2015](#)) and UCH II regions (e.g. [Hanson et al. 2002](#)). While fitting model SEDs, we adopted an error of 10, 15 and 20 per cent, respectively, for the UKDISS, *Spitzer* and $70 \mu\text{m}$ fluxes instead of formal photometric errors in order to fit without possible bias that may cause by underestimation of the flux uncertainties. Figure 5 shows the model SEDs of 14 sources for which we have reasonable number of data points between 1.2 to $70 \mu\text{m}$. As can be seen, although SED models show some degree of degeneracy, they appear to fit the data reasonably well. Barring source 26 (i.e. the driving source of MHO 2333), all the SED models clearly show rising SEDs up to $70 \mu\text{m}$, consistent with our earlier classifications that majority of them are protostars.

Like any other models, these models have their own sets of limitations. For example, these models do not account for interstellar radiation fields (IRSF), cold dust of the protostellar envelopes (i.e. dust below 30 K) and stellar multiplicity, etc. The main objective here is not to provide a precise set of physical parameters for the YSOs but to find the range of a few key parameters from the models and then discuss the possible nature of the sources. To do so, we obtained physical parameters of the sources by adopting the approach similar to [Robitaille et al. \(2007\)](#), i.e.

by considering those models satisfy $\chi^2 - \chi_{\min}^2 \leq 2N_{\text{data}}$, where χ_{\min}^2 is the goodness-of-fit parameter for the best-fitting model and N_{data} is the number of input observational data points. We then obtained the parameters from the weighted mean and standard deviation of these best-fitting models weighted by $e^{(-\chi^2/2)}$ (e.g. Samal et al. 2012). These parameters are tabulated in Table. 2, including the stellar mass (M_*), stellar age (t_*), disc mass (M_{disc}) disc accretion rate (\dot{M}_{disc}) and total luminosity (L_{bol}) of each source. As per the models, the disc masses are in the range $0.003 - 0.14 M_{\odot}$ with a median $\sim 0.02 M_{\odot}$, disc accretion rates are in the range $0.08 - 9.7 \times 10^{-7} M_{\odot} \text{ yr}^{-1}$ with a median $\sim 2.8 \times 10^{-7} M_{\odot} \text{ yr}^{-1}$, and age in the range $0.05 - 3 \times 10^5 \text{ yr}$, with a median value $\sim 1 \times 10^5 \text{ yr}$.

Figure 6(a) shows the disc masses of the YSOs obtained in the present work (blue dots) and their comparison with those in the nearby star-forming regions (Williams & Cieza 2011), measured through sub(mm) observations. In Fig 6(a), the solid line represents the median ratio of disc to stellar mass, i.e. ~ 1 per cent as derived by Williams & Cieza (2011) from the compilation of a large number of class II/III YSOs in the stellar mass range $0.4 - 10 M_{\odot}$, and the shaded area represents the 1 dex spread about the median value of their sample. Similarly, Fig. 6(b) shows the disc accretion rates of the YSOs obtained in the present work (blue dots) and their comparison with the literature values of the nearby star-forming regions as compiled by Hartmann et al. (2016). These authors compiled a large number of class II/III YSOs, for which accretion rates are measured in various ways (e.g. spectroscopic measurements of the Balmer continuum, photometric U -band measurements and emission line measurements) and observed a strong correlation with stellar-mass. In Fig. 6(b), the solid line represents the relation, $\dot{M}_{\text{disc}} \propto M_*^{2.1}$, obtained by Hartmann et al. (2016), and the shaded area represents the 3σ scatter around this line, where σ is ~ 0.75 dex (see Hartmann et al. 2016, for detailed discussion).

As can be seen from Fig. 6, despite the evolutionary difference between the sources (i.e. protostars versus class II/III YSOs), in general, the SED model based disc measurements show a fair agreement with the literature values at any given stellar mass, indicating that the obtained disc properties of the driving sources may be the representation of their true values. In the absence of high-resolution mm observations and precise extinction measurements, we emphasize that the obtained disc parameters are still indicative and should be treated with caution. On the other hand, as one can see from Fig. 5, for a given source the overall shape of all the models in general is similar, so bolometric luminosities of the sources are expected to be better constrained. In fact, we find they are in reasonable agreement with luminosity estimated based on the $70 \mu\text{m}$ flux alone (discussed in Section 4.2.2).

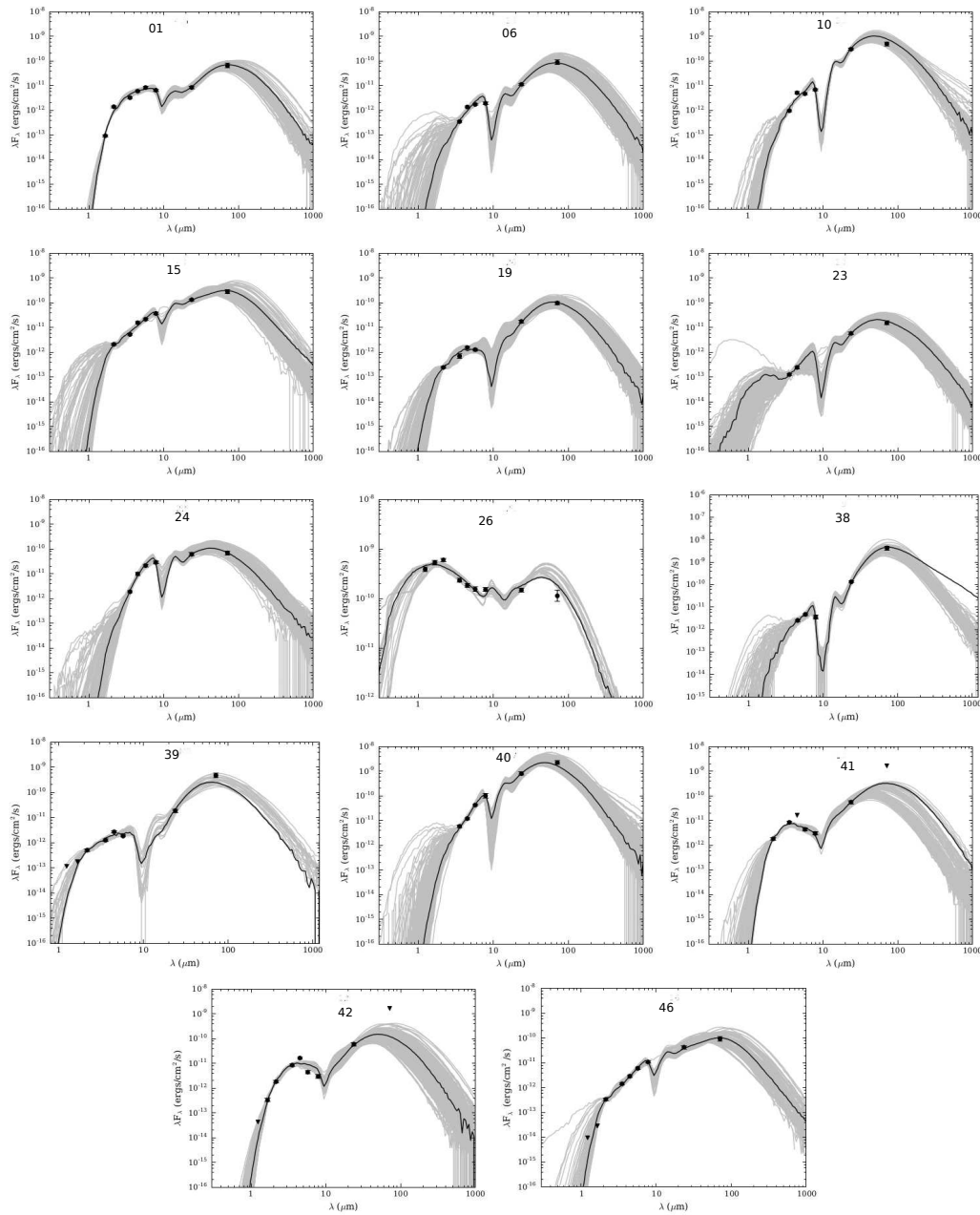
18 *Samal et al.*

Figure 5. The observed SEDs of the driving sources and their best-fit models. The ID numbers correspond to the entries in the first column of Table. 1. The black line shows the best-fitting model, and the grey-lines show subsequent best-fitting models that satisfy $\chi^2 - \chi_{\min}^2 \leq 2N_{\text{data}}$ criteria. Filled circles and triangles show the ‘data points’ and ‘upper-limits’ respectively. The IDs correspond to the MHO names given in Table. 1.

4.2.2 Luminosity of the driving sources using only 70 μm flux

[Dunham et al. \(2006\)](#) using radiative transfer models demonstrated that 70 μm is a crucial wavelength for determining L_{bol} for embedded protostars, as radiative transfer models are strongly constrained by this wavelength, and it is largely unaffected by the details of the source geometry and external heating. Furthermore, [Dunham et al. \(2008\)](#) examined c2d protostars and obtained the following tight correlation between L_{bol} (excluding luminosity arising from external heating)

Table 2. Inferred Physical Parameters from the SED modeling

ID	M_* (M_\odot)	age (10^5 yr)	M_{disc} (M_\odot)	\dot{M}_{disc} ($10^{-8} M_\odot/\text{yr}$)	L ($10^2 L_\odot$)
01	2.10 ± 0.87	1.56 ± 0.90	0.049 ± 0.073	0.004 ± 0.009	0.27 ± 0.06
06	1.75 ± 0.70	0.99 ± 0.68	0.007 ± 0.009	0.021 ± 0.064	0.26 ± 0.09
10	4.13 ± 0.70	0.14 ± 0.26	0.099 ± 0.057	0.824 ± 0.646	2.52 ± 0.17
15	1.45 ± 0.62	0.15 ± 0.31	0.077 ± 0.037	0.578 ± 0.630	0.53 ± 0.22
19	2.07 ± 0.53	1.32 ± 0.64	0.011 ± 0.013	0.009 ± 0.020	0.34 ± 0.09
23	0.96 ± 0.31	0.86 ± 0.69	0.013 ± 0.013	0.036 ± 0.097	0.13 ± 0.04
24	1.00 ± 0.32	0.05 ± 0.28	0.007 ± 0.012	0.504 ± 0.942	0.35 ± 0.13
26	5.85 ± 0.17	2.77 ± 0.77	0.065 ± 0.042	0.003 ± 0.003	2.86 ± 0.44
38	4.58 ± 2.50	0.04 ± 0.07	0.141 ± 0.107	97.49 ± 95.73	7.15 ± 1.57
39	5.07 ± 0.61	2.10 ± 0.63	0.006 ± 0.016	0.001 ± 0.003	1.47 ± 0.43
40	6.51 ± 1.75	0.78 ± 0.71	0.126 ± 0.146	20.39 ± 40.12	8.27 ± 2.06
41	4.60 ± 0.26	1.40 ± 0.08	0.015 ± 0.010	0.005 ± 0.001	0.92 ± 0.06
42	4.22 ± 0.79	2.76 ± 1.10	0.003 ± 0.007	0.001 ± 0.004	0.70 ± 0.14
46	1.15 ± 0.31	0.25 ± 0.17	0.020 ± 0.017	0.067 ± 0.152	0.20 ± 0.06

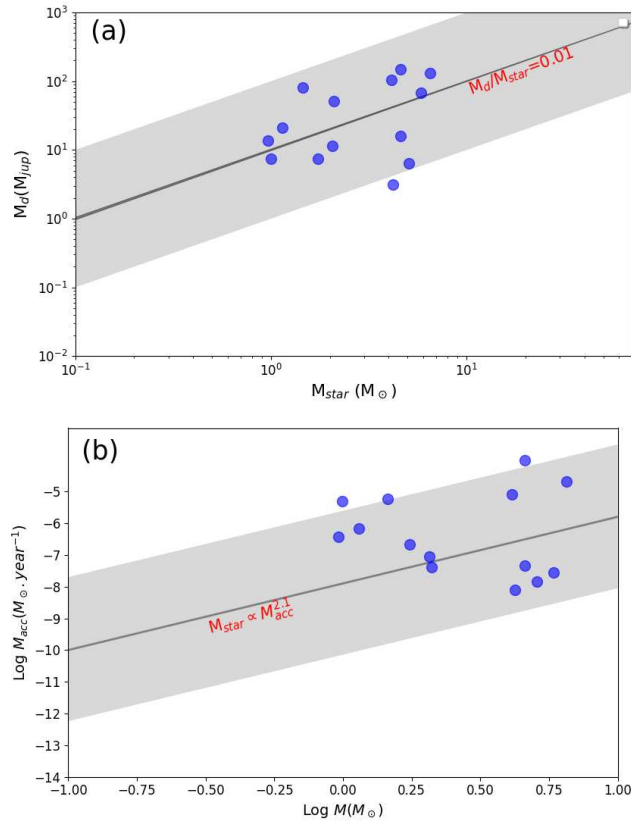


Figure 6. (a): Variation of protoplanetary disc mass (in the unit of Jupiter mass) with the mass of the central star. (b): Correlation between stellar-mass and accretion rate. In both plots, our SED model based measurements are shown in blue dots, while the solid line and the shaded area represent the measurements from literature for the class II/III YSOs and have the same meaning as described in the text.

and F_{70} for low-luminosity protostars:

$$L_{\text{bol}} = 3.3 \times 10^8 F_{70}^{0.94} (d/140pc)^2 L_\odot, \quad (1)$$

where F_{70} is in cgs units ($\text{erg cm}^{-2} \text{s}^{-1}$). While this method is accurate within a factor of 2 to 3 (e.g. Dunham et al. 2008; Commerçon et al. 2012), it offers a proxy way of obtaining L_{bol} for embedded protostars. It is worth noting that, Ragan et al. (2012), have shown that the $70 \mu\text{m}$ flux of more massive sources also correlates well with their total luminosity and there is a good agree-

20 *Samal et al.*

ment between the correlations established for low and high-luminosity sources. Among our YSO sample, five sources have detection only in 24 and 70 μm , or in 70 μm , on which we could not perform SED modeling. We therefore used the above empirical relationship for obtaining bolometric luminosity of these candidates. Of these, four are found to be in the range of $\sim 4\text{--}53 L_{\odot}$, and one is exceptionally luminous with luminosity $\sim 0.5 \times 10^4 L_{\odot}$. The latter source corresponds to an extremely young YSO associated to an EGO (see Section 5.1 for further discussion). The luminosity of these sources is also tabulated in Table. 2. We compared the 70 μm flux based and SED model based luminosities for common protostars (i.e. class 0/I), and found that two estimates are in agreement with each other within a factor of 2.

From the luminosity and the disc properties of the driving sources, we can say that most of them are intermediate-mass young stellar objects (for mass-luminosity relationship of protostars, see Fig. 4 of [André et al. \(2008\)](#) and references therein) that are still actively accreting from their protoplanetary disc. We note, outflow power is strongly correlated to YSO luminosity (e.g. [Caratti o Garatti et al. 2015](#)), therefore the predominance of moderate-mass YSOs in our sample of driving sources could be a selection effect caused by sensitivity of the *Spitzer* and *Herschel* images at the distance of M17.

5 DISCUSSION

5.1 Notes on general nature of the MHOs and discussion on a few types of interesting sources

In this work, we have identified 48 MHOs. Of which, 45 (93 per cent) MHOs are new discoveries. Of the three already known outflows, two (MHO 2306 and MHO 2344) have been identified by [Cyganowski et al. \(2008\)](#) as EGOs using *Spitzer* observations and one (i.e. MHO 2307) by [Caratti o Garatti et al. \(2015\)](#) using 2.12 μm observations. This shows the improvement UWISH2 can bring when it comes to identify outflows over galactic scales.

Out of 48 MHOs, we could only associate 20 YSO candidates. This corresponds to 40 per cent of all the MHOs. If we consider the dust cores and clusters as the potential driving sources, the number of sources increases to 30 which is ~ 60 per cent of all the MHOs. We could not link the remaining MHOs with any potential YSO candidates, which could either be due to indistinct shock orientation with respect to the nearby YSOs or shocks are from distant sources or shocks are from low-luminosity sources beyond our sensitivity limit ($< 3 L_{\odot}$; discussed below). But largely the situation here is similar to Serpens and Aquila ([Ioannidis & Froebrich 2012a](#)), Orion A ([Davis](#)

et al. 2009), Vela C (Zhang et al. 2014) and Cygnus-X (Makin & Froebrich 2018), where only 50 to 60 per cent of the MHOs were found to have associated YSOs.

From SED models or using only 70 μm fluxes, we find that the outflows are mostly driven by sources of luminosity in the range 4–1000 L_{\odot} , suggesting that more low-to-intermediate mass YSOs with outflows can be studied and characterized over larger distances with the help of UWISH2 survey.

In our sample, five (MHO 2306, MHO 2328, MHO 2329, MHO 2331, MHO 2337 and MHO 2343) out of the 20 YSOs have no detection in 5.8 and/or 8.0 μm bands in the MIPS GAL catalogue, yet were detected in 24 and/or 70 μm . Our findings suggest that search for outflow driving source without 24 and 70 μm would result in missing many potential candidates (e.g. ~ 30 per cent in the present case). 24 μm is an important wavelength for determining whether a source features a rising (or falling) SED. 70 μm is particularly important for the identification of very young protostars and perhaps even for first hydro static cores (e.g. Enoch et al. 2010). We find as protostars are bright at mid- and far-infrared, in the multi-colour IRAC-MIPS images the outflow-driving sources clearly stand out compared to the nearby sources (e.g. see Figures in Appendix B).

In our sample (see Table. 1), although the majority of the bipolar outflows have a total length less than 0.4 pc, the MHO 2347, however, corresponds to a parsec-scale outflow (see Fig. 7) from a class 0 source. We note, Caratti o Garatti et al. (2015) have also observed MHO 2347, but only part of it. With our sensitive observations we detect additional three knots along the southwestern lobe of MHO 2347, which makes it the largest H_2 outflow of the M17 complex. We find the outflow shows some degree of bend morphology and consists of a series of compact knots at a median spacing of ~ 0.15 pc (for details see Appendix B). Episodic ejection of material by quasi-periodic outbursts of the central star-disc system is one of the possible explanation of regular spacing between the knots (e.g. Raga et al. 2010). Recently, Vorobyov & Basu (2015) using hydrodynamical simulations showed that episodic accretion events induced by gravitational instabilities and disc fragmentation, are present mainly during the early evolution (class 0) of most protostellar systems. In addition to bursts induced by disc instabilities, it has also been suggested that bursts can be induced by external interactions with one or more companion stars. So objects like MHO 2347 are of particular interest for studying the accretion history and cause of variability in very young systems (e.g. see discussion in Meyer et al. 2017; Herczeg et al. 2017; Caratti o Garatti et al. 2017).

In our list, we find that MHO 2306 corresponds to an EGO (details given in Appendix B). This MHO has been identified by Lee et al. (2012) using UWISH2 images while searching for

22 *Samal et al.*

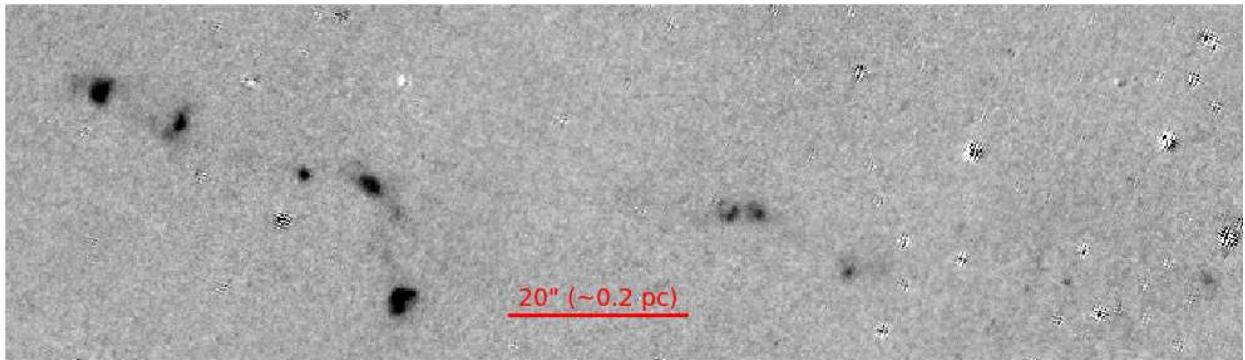


Figure 7. Continuum subtracted H_2 image of the MHO 2347, showing chain of knots spread over parsec-scale. We note, the bright bow-shock shaped knot seen at the central bottom part of the figure is part of MHO 2307.

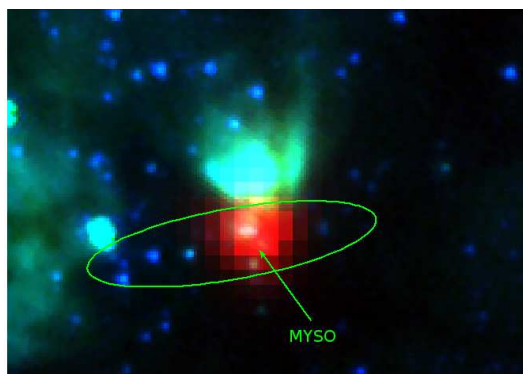


Figure 8. Color composite image around MHO 2306 at 3.6 (blue), 8.0 (green) and 70 μm (red). The ellipse denotes the flow axis of the MHO 2306 (for details see Appendix B). The arrow points to the 70 μm bright MYSO, the likely source responsible for MHO 2306.

EGOs counterpart in H_2 . We find a bright 70 μm point source at location of EGO. The source location also coincides with the location of a methanol maser (Bayandina et al. 2012) which is a tracer of early evolutionary stages of high-mass star formation (Ellingsen 2006). The source lies adjacent to a compact H II region that is bright at 8 and 24 μm (see Fig. 8) and has no 24 μm counterpart in the MIPS GAL catalogue. It is embedded in a clump of column density $\sim 7 \times 10^{23} \text{ cm}^{-2}$ (Tang et al. 2017), thus in a region of very high extinction. Its 70 μm flux suggests to a source of luminosity $\sim 0.5 \times 10^4 L_{\odot}$, however, no associated radio free-free emission at 5 GHz (resolution ~ 1.5 arcsec and rms ~ 0.4 mJy) is found in the CORNISH⁶ survey image (Hoare et al. 2012). It appears that, although its luminosity represents a high-mass star, it is yet to develop an UCH II region. Thus represents a young massive YSO with an outflow. Similarly, MHO 2344 (driven by a $\sim 700 L_{\odot}$ class 0 type YSO) present a case where multiple wide-angle bullets have been observed (see Fig. and Section 4.1 for details). We suggest, these massive YSOs are potential candidates for studying various aspects of early phases of massive star-formation and evolution (e.g. see discussion in Tan et al. 2016; Bally et al. 2017).

⁶ <http://cornish.leeds.ac.uk/public/index.php>

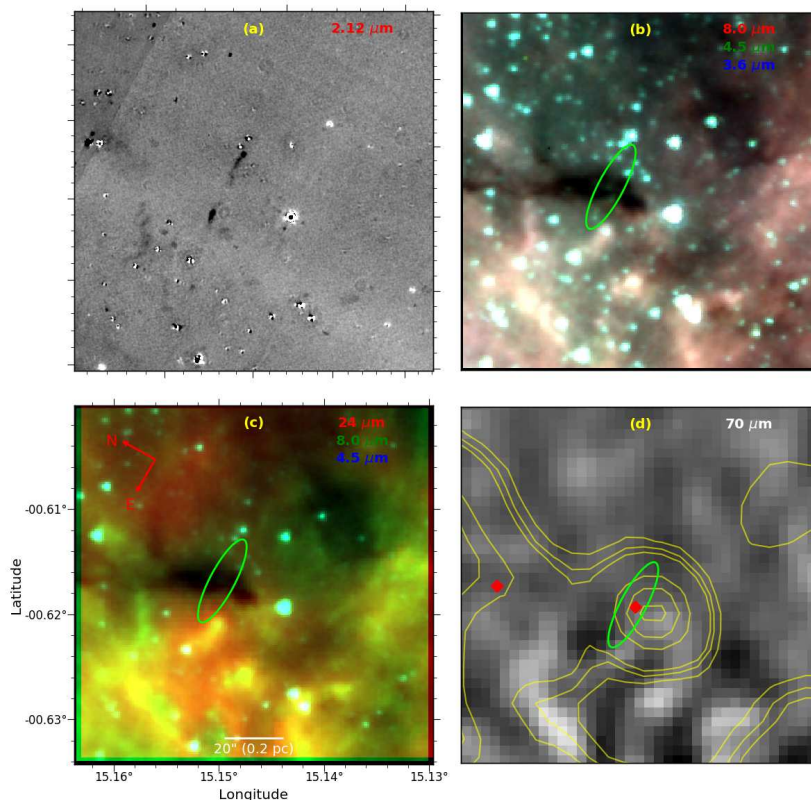


Figure 9. Multicolour image around the MHO 2352, showing the emergence of H_2 jets from a *Spitzer* dark-cloud, with no embedded point sources up to $70 \mu\text{m}$. The colour codings have the same meaning as in Fig. 3. The diamond symbols on the $70 \mu\text{m}$ image represent the SCUBA cores. The $870 \mu\text{m}$ contours are shown in orange colours.

We identified H_2 jets and knots in the vicinity of six $70 \mu\text{m}$ dark cores (MHO 2335, MHO 2338, MHO 2341, MHO 2350, MHO 2352 and MHO 2353), but for three cases (MHO 2341, MHO 2350 and MHO 2352), we observed symmetric jets clearly emanating from the cores located at the middle of the jet axis. Figure 9 illustrates an example. As can be seen, the MHO consists of two strong opposite jets. Together, they delineate a north-south outflow. In the *Spitzer* bands, a dark-cloud perpendicular to the flow axis, can be seen as an absorption feature against the bright background. The morphology and the compactness of the jets strongly suggest that a driving source should be embedded inside the dark-cloud. No point sources were found between 3.6 to $70 \mu\text{m}$ in the dark-cloud along the axis of the jets. However, one can see a SCUBA core (mass $\sim 9 M_\odot$; Reid & Wilson (2006)) lies at the expected location. Thus, the core is the most likely source responsible for the jets. Most of the driving sources identified in this work are bright in mid-IR and visible in $70 \mu\text{m}$. The 3σ point-source sensitivity of the $70 \mu\text{m}$ image is $\sim 0.24 \text{ Jy}$, where σ is the standard deviation of the background intensity. Using equation (1), 0.24 Jy corresponds to a luminosity $\sim 3 L_\odot$. Thus, we cannot ignore the possibility that the starless cores may in fact harbor faint YSOs of luminosity $< 3 L_\odot$. At this point, we are ill-qualified to comment whether these $70 \mu\text{m}$ dark cores are starless or protostellar. None the less, these mid- and far-infrared quiet clumps/cores are

24 *Samal et al.*

potential targets for the understanding of early phases of core collapse and fragmentation (e.g. see discussion in [Traficante et al. 2018](#); [Palau et al. 2018](#)).

5.2 Dominant YSO class responsible for the jets

The present H₂ survey cover a small area about 1.5 square degree, but it is worthwhile to compare our results with the results from other similar surveys of nearby star-forming regions to understand at what stage of protostellar evolution H₂ jets are prominent. In the present work, we find that of the 20 YSOs with outflows, 18 (~90 per cent) outflows are driven by protostars (i.e, class 0/I YSOs), which is similar to the ≥ 80 per cent of the H₂ outflows in Orion A ([Davis et al. 2009](#)), ~ 90 per cent in Corona Australis ([Kumar et al. 2011](#)), ≥ 90 per cent in Serpens South ([Teixeira et al. 2012](#)), ~ 70 per cent in Aquila ([Zhang et al. 2015](#)) and ~ 80 per cent in Cygnus-X ([Makin & Froebrich 2018](#)) molecular clouds, except the Cassiopeia and Auriga complex ([Froebrieh & Makin 2016](#)) where 20 per cent of the driving sources are protostars, the remainder are Classical T-Tauri Stars. The above trend (except Cassiopeia and Auriga complex) hints that the H₂ jets are mostly prominent in class 0/I type protostars and the jet activity possibly decreases significantly as the object evolves. However, we stress that the above trend can be biased by the selection effect as older sources tend to reside in relatively molecule-free environments, and thus their shocks may not be traced by MHOs. Sensitive optical observations at H _{α} and [SII] lines would be helpful to solidify the above trend.

5.3 Jet lengths and dynamical time scales

Figure 10 shows the frequency distribution of total length of the outflows that are associated either with a YSO or a core. Here, we assume that the total length of a monopolar appearance outflow is twice of its single-sided lobe length (the distance of the farthest H₂ feature from the YSO/core), while it is end-to-end for bipolar outflows. Using this simple approach, we find that the total outflow lengths of the MHOs are in the range of 0.05 pc to 1.2 pc, with a median ~ 0.34 pc.

We note that these lengths refer to the lengths of the visible H₂ jets, not necessarily the total lengths of the flows, as outflow length depends on many factors such as the tracer in question, inclination angle to the line of sight, the density of the ambient medium, etc., so more extreme values may be feasible. [Froebrieh & Makin \(2016\)](#) argued that, since bipolar outflows are often asymmetric, measuring outflow lengths in the traditional way (from end-to-end) should be avoided. Owing to low statistics of the outflow sources, here we did not measure the length of each lobe

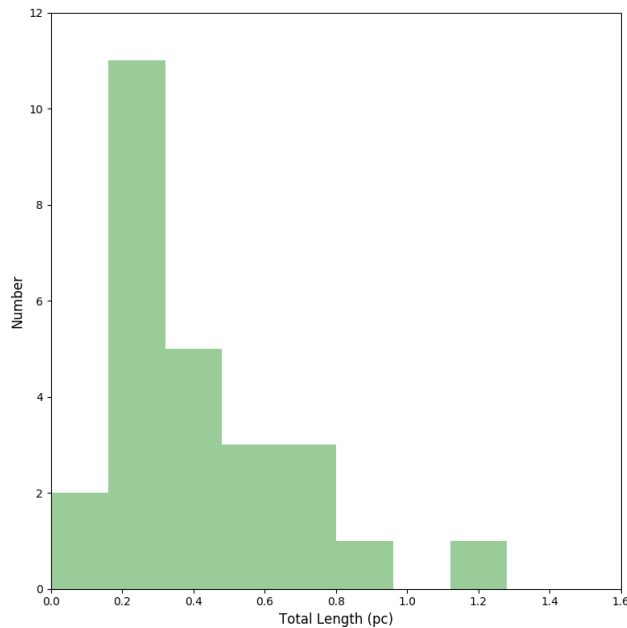


Figure 10. Total length distribution of the outflows that are either associated with a YSO or a core.

separately. None the less, if we consider the length of the longest lobe as the true half length of a bipolar flow, then we find the total outflow lengths of all the MHOs are in the range of 0.09 pc to 1.6 pc, with a median ~ 0.44 pc. We would like to point that outflows can break-out of their parent clumps and interact with medium of little molecular gas; thus, the MHO-based outflow sizes can be limited by the spatial extent of the molecular cloud, hence are likely representative of lower-bounds of the true extent of the flows. We estimated the likely lower-limits of the dynamical time-scales (t_{dyn}) of the outflows using the relation $t_{dyn} = D/(V \sin i)$, where D is the length of the lobe, V is the velocity of the jets, and i is the inclination of the outflow with respect to the line of sight. Here we assume an average flow inclination angle $\sim 57^\circ.3$ (see discussion in [Bontemps et al. 1996](#)), a flow velocity $\sim 35 \text{ km s}^{-1}$ which is the median value of 86 H_2 features measured by [Zhang et al. \(2013\)](#) using proper motion observations, and jets travel with a constant velocity since their launch. Under these assumptions, we find that the time-scales of ejection are in the range $0.01\text{--}0.2 \times 10^5$ yr, with a median $\sim 0.07 \times 10^5$ yr. The median time-scale is slightly lower than the lifetime of the class 0/I sources ($\sim 0.4 \times 10^5$ yr; [Evans et al. 2009](#)) and the median age of the YSOs as estimated from the SED modeling. Proper velocity and size measurements, and inclination angle of the jets would shed more light on the correlation between the dynamical time-scale and lifetime of the protostars.

26 *Samal et al.*

6 GENERAL PICTURE OF STAR FORMATION IN THE M17 COMPLEX

As discussed in Section 5.2, jets are possibly more prominent in the class 0/I phase of a YSO. Thus the distribution of H₂ jets/knots offers an independent diagnostic to trace the recent star formation activity of a complex. Fig. 2a shows relative spatial distribution of the MHOs and the cold gas at 870 μm . As can be seen, the cold dust emission (red contours) mainly corresponds to the absorption features of the background 24 μm image, and primarily concentrated at the location of A, B, C and D components of the complex. Also most of the MHOs are located in the close vicinity of the intense 870 μm emission, and they show a good correlation with the distribution of SiO emission (see Fig. 2b). We observed that in 70 per cent of the cases, the clump with a SiO emission coincides with an MHO, suggesting active star-formation is ongoing in these clumps. Looking at the large-scale spatial distribution of MHOs and 870 μm dust emission, it appears that M17 complex consists of several scattered star-forming clumps with jets and SiO emission, separated by distances of several parsecs from each other. This suggests the hierarchical nature of the molecular cloud (e.g. see discussion in [Vázquez-Semadeni et al. 2017](#); [Caldwell & Chang 2018](#)).

One can also notice that among the structures of M17, M17SWex is filamentary and H₂ flows are more abundant in its direction, compared to other parts of the complex. Using high-resolution NH₃ and 1.3 millimeter observations, dense filamentary clouds with density as high as $\sim 10^{23}$ cm⁻² have been observed in M17SWex ([Busquet et al. 2013, 2016](#)). This high column of matter could have limited our ability to detect some of the weaker flows compared to the less extincted regions of the complex. Even so, based on the distribution of the MHOs, largely it appears that M17SWex is currently forming stars actively among all the fragments, thereby supporting the fact that in molecular clouds filaments and filamentary structures are prime sites of active star formation (e.g. [Könyves et al. 2015](#); [Samal et al. 2015](#); [Ryabukhina et al. 2018](#)). We find our results are in accordance with the results obtained by [Povich & Whitney \(2010\)](#); [Povich et al. \(2016\)](#), [Busquet et al. \(2013\)](#) and [Busquet et al. \(2016\)](#) for M17SWex. These authors using multiwavelength observations found that the M17SWex region is associated with a rich number of YSOs/cores, and suggest that it may form many more stars by accreting a significant amount of surrounding gas fed by the filaments.

In contrast to M17SWex, in the interior of the H II region, we observed only a few MHOs – which is not surprising, given the fact that it hosts a 3 Myr old cluster (cluster centre is marked with a star symbol in the figure), where one would expect a low-fraction of sources with active accretion

disc (e.g. [Jose et al. 2017](#)). This implies that star formation has stopped or is in a more advanced phase in the central region of the M17. The presence of a significant amount of $870\ \mu\text{m}$ cold dust and a small number of outflows (either MHOs or SiO emission) surrounding the H II region (particularly in the fragment 'B'), however, suggests that a very early phase of star formation is still ongoing at the periphery of the H II region. We suggest that these outflows are probably from the second generation young stars whose formation has been triggered by the compression of the expanding H II region, as observed at the borders of several Galactic H II regions (e.g. [Getman et al. 2012](#); [Panwar et al. 2014](#); [Samal et al. 2014](#); [Deharveng et al. 2015](#); [Bernard et al. 2016](#)). In fact, strong evidence of M17SW and nearby molecular clouds are heated and compressed by the H II region has been observed using molecular observations (e.g. [Lada 1976](#); [Wilson et al. 2003](#)).

All in all, in the M17 complex, M17SWex, appears to be the most active site of star formation, representing an excellent cloud for understanding the early phases of cluster formation and evolution under the influence of strong outflow feedback.

7 SUMMARY

In this work, we use the infrared observations of the H_2 1-0 S(1) line at $2.12\ \mu\text{m}$, with the UKIDSS, *Spitzer* and *Herschel* maps in the wavelength range $1.2\text{--}70\ \mu\text{m}$ to identify protostars with jets and knots in the M17 complex as well as to understand its ongoing star formation activity.

We identified 48 MHOs over $2.0^\circ \times 0.8^\circ$ area of the complex, i.e. potential outflow candidates, ~ 93 per cent of which are new discoveries. Based on the alignments and morphologies of the MHOs with the nearby YSO candidates, we could associate 20 YSO candidates to the outflows. Using various flux ratios, we deduce an evolutionary status of these candidates and find that ~ 90 per cent of the driving sources are protostars (i.e. class 0/I), and only ~ 10 per cent of the MHOs are driven by class II YSOs. Among the protostar, three are likely PBRs.

Using the grid models of [Robitaille et al. \(2006\)](#), we matched the model spectral energy distributions to the observed SEDs of the 14 outflow driving YSOs. This allows for the estimation of the physical properties such as mass, luminosity, and accretion rate of the protostars. We find that the disc masses and disc accretion rates of ~ 80 per cent YSOs are in the range $0.003\text{--}0.14\ M_\odot$ and $0.08\text{--}9.7 \times 10^{-7}\ M_\odot\ \text{yr}^{-1}$, respectively. From SED modeling and using only $70\ \mu\text{m}$ flux, we estimated that the outflows are mostly driven by sources of luminosity in the range $4\text{--}1000\ L_\odot$, suggesting that more low-to-intermediate mass YSOs with outflows can be studied and characterized over larger distances with the help of UWISH2 survey.

28 *Samal et al.*

Our results show that six outflows are possibly emanating from cores, where, no infrared sources were detected up to $70 \mu\text{m}$. These sources are important targets for follow-up studies for the understanding of the very early phase of star-formation.

We observed a parsec scale bipolar outflow from a class 0 YSO with regularly spaced knots, a potential candidate for understanding the variability in very young systems. We also observed a strong spatial correlation between H_2 jets/knots and SiO emission for massive ATLASGAL clumps.

Among the structures of M17, we find that H_2 jets/knots are statistically more numerous in the M17SWex region of the complex. Since H_2 emission is a tracer of recent ejecta from young protostars, we suggest that in the M17 complex, currently M17SWex is the most active region of star formation and is an excellent template for the understanding of the early evolution of young clusters that are under the influence of strong outflow feedback.

ACKNOWLEDGMENTS

We are grateful to the anonymous referee for useful comments that have helped us to improve the scientific contents of the paper. M.R. Samal acknowledges the Ministry of Science and Technology of Taiwan for his post-doctoral fellowship. The data reported here were obtained as part of the UKIRT Service Program.

REFERENCES

- Aguirre J. E., et al., 2011, *ApJS*, **192**, 4
- Allen L. E., et al., 2004, *ApJS*, **154**, 363
- André P., et al., 2008, *A&A*, **490**, L27
- Arce H. G., Shepherd D., Gueth F., Lee C.-F., Bachiller R., Rosen A., Beuther H., 2007, *Protostars and Planets V*, pp 245–260
- Aso Y., et al., 2017, *ApJ*, **850**, L2
- Bally J., 2007, *Ap&SS*, **311**, 15
- Bally J., Cunningham N. J., Moeckel N., Burton M. G., Smith N., Frank A., Nordlund A., 2011, *ApJ*, **727**, 113
- Bally J., Ginsburg A., Probst R., Reipurth B., Shirley Y. L., Stringfellow G. S., 2014, *AJ*, **148**, 120
- Bally J., Ginsburg A., Silvia D., Youngblood A., 2015, *A&A*, **579**, A130
- Bally J., Ginsburg A., Arce H., Eisner J., Youngblood A., Zapata L., Zinnecker H., 2017, *ApJ*, **837**, 60
- Balog Z., et al., 2014, *Experimental Astronomy*, **37**, 129
- Bayandina O. S., Val'tts I. E., Larionov G. M., 2012, *Astronomy Reports*, **56**, 553
- Benjamin R. A., et al., 2003, *PASP*, **115**, 953
- Bernard A., Neichel B., Samal M. R., Zavagno A., Andersen M., Evans C. J., Plana H., Fusco T., 2016, *A&A*, **592**, A77
- Bhavya B., Subramaniam A., Kuriakose V. C., 2013, *MNRAS*, **435**, 663
- Bontemps S., André P., Terebey S., Cabrit S., 1996, *A&A*, **311**, 858
- Broos P. S., et al., 2013, *ApJS*, **209**, 32

- Busquet G., et al., 2013, *ApJ*, 764, L26
- Busquet G., et al., 2016, *ApJ*, 819, 139
- Cabrit S., 2007, in Bouvier J., Appenzeller I., eds, IAU Symposium Vol. 243, Star-Disk Interaction in Young Stars. pp 203–214, doi:10.1017/S1743921307009568
- Caldwell S., Chang P., 2018, *MNRAS*, 474, 4818
- Caratti o Garatti A., Stecklum B., Linz H., Garcia Lopez R., Sanna A., 2015, *A&A*, 573, A82
- Caratti o Garatti A., et al., 2017, *Nature Physics*, 13, 276
- Carey S. J., et al., 2009, *PASP*, 121, 76
- Carney M. T., Yıldız U. A., Mottram J. C., van Dishoeck E. F., Ramchandani J., Jørgensen J. K., 2016, *A&A*, 586, A44
- Chapman N. L., Mundy L. G., Lai S.-P., Evans II N. J., 2009, *ApJ*, 690, 496
- Chini R., Elsaesser H., Neckel T., 1980, *A&A*, 91, 186
- Codella C., Cabrit S., Gueth F., Cesaroni R., Bacciotti F., Lefloch B., McCaughrean M. J., 2007, *A&A*, 462, L53
- Commerçon B., Launhardt R., Dullemond C., Henning T., 2012, *A&A*, 545, A98
- Crapsi A., van Dishoeck E. F., Hogerheijde M. R., Pontoppidan K. M., Dullemond C. P., 2008, *A&A*, 486, 245
- Csengeri T., et al., 2014, *A&A*, 565, A75
- Csengeri T., et al., 2016, *A&A*, 586, A149
- Cyganowski C. J., et al., 2008, *AJ*, 136, 2391
- Cyganowski C. J., Brogan C. L., Hunter T. R., Churchwell E., 2009, *ApJ*, 702, 1615
- Davis C. J., Kumar M. S. N., Sandell G., Froebrich D., Smith M. D., Currie M. J., 2007, *MNRAS*, 374, 29
- Davis C. J., et al., 2009, *A&A*, 496, 153
- Davis C. J., Gell R., Khanzadyan T., Smith M. D., Jenness T., 2010, *A&A*, 511, A24
- De Buizer J. M., Vacca W. D., 2010, *AJ*, 140, 196
- Deharveng L., et al., 2015, *A&A*, 582, A1
- Dunham M. M., et al., 2006, *ApJ*, 651, 945
- Dunham M. M., Crapsi A., Evans II N. J., Bourke T. L., Huard T. L., Myers P. C., Kauffmann J., 2008, *ApJS*, 179, 249
- Dunham M. M., et al., 2015, *ApJS*, 220, 11
- Ellingsen S. P., 2006, *ApJ*, 638, 241
- Elmegreen B. G., Lada C. J., Dickinson D. F., 1979, *ApJ*, 230, 415
- Enoch M. L., Evans II N. J., Sargent A. I., Glenn J., 2009, *ApJ*, 692, 973
- Enoch M. L., Lee J.-E., Harvey P., Dunham M. M., Schnee S., 2010, *ApJ*, 722, L33
- Evans II N. J., et al., 2009, *ApJS*, 181, 321
- Feng S., Beuther H., Zhang Q., Liu H. B., Zhang Z., Wang K., Qiu K., 2016, *ApJ*, 828, 100
- Froebrich D., Makin S. V., 2016, *MNRAS*, 462, 1444
- Froebrich D., et al., 2011, *MNRAS*, 413, 480
- Froebrich D., et al., 2015, *MNRAS*, 454, 2586
- Georgelin Y. M., Georgelin Y. P., Roux S., 1973, *A&A*, 25, 337
- Gerin M., Pety J., Fuente A., Cernicharo J., Commerçon B., Marcelino N., 2015, *A&A*, 577, L2
- Getman K. V., Feigelson E. D., Sicilia-Aguilar A., Broos P. S., Kuhn M. A., Garmire G. P., 2012, *MNRAS*, 426, 2917
- Gibb A. G., Richer J. S., Chandler C. J., Davis C. J., 2004, *ApJ*, 603, 198
- Guesten R., Fiebig D., 1988, *A&A*, 204, 253
- Gutermuth R. A., Heyer M., 2015, *AJ*, 149, 64
- Gutermuth R. A., et al., 2008, *ApJ*, 674, 336
- Gutermuth R. A., Megeath S. T., Myers P. C., Allen L. E., Pipher J. L., Fazio G. G., 2009, *ApJS*, 184, 18
- Hanson M. M., Luhman K. L., Rieke G. H., 2002, *ApJS*, 138, 35
- Hartmann L., Calvet N., Gullbring E., D'Alessio P., 1998, *ApJ*, 495, 385
- MNRAS **000**, ??–?? (2018)

30 *Samal et al.*

- Hartmann L., Herczeg G., Calvet N., 2016, *ARA&A*, 54, 135
- Heiderman A., Evans II N. J., 2015, *ApJ*, 806, 231
- Helfand D. J., Becker R. H., White R. L., Fallon A., Tuttle S., 2006, *AJ*, 131, 2525
- Herczeg G. J., et al., 2017, *ApJ*, 849, 43
- Hoare M. G., et al., 2012, *PASP*, 124, 939
- Hodapp K. W., 2007, *AJ*, 134, 2020
- Hoffmeister V. H., Chini R., Scheyda C. M., Schulze D., Watermann R., Nürnberger D., Vogt N., 2008, *ApJ*, 686, 310
- Hosokawa T., Omukai K., 2009, *ApJ*, 691, 823
- Ioannidis G., Froebrich D., 2012a, *MNRAS*, 421, 3257
- Ioannidis G., Froebrich D., 2012b, *MNRAS*, 425, 1380
- Jiang Z., et al., 2002, *ApJ*, 577, 245
- Joncas G., Roy J.-R., 1986, *ApJ*, 307, 649
- Jose J., Herczeg G. J., Samal M. R., Fang Q., Panwar N., 2017, *ApJ*, 836, 98
- Khanzadyan T., et al., 2012, *A&A*, 542, A111
- Könyves V., et al., 2015, *A&A*, 584, A91
- Kumar M. S. N., Sharma S., Davis C. J., Borissova J., Grave J. M. C., 2011, *A&A*, 533, A137
- Lada C. J., 1976, *ApJS*, 32, 603
- Lada C. J., 1987, in Peimbert M., Jugaku J., eds, IAU Symposium Vol. 115, Star Forming Regions. pp 1–17
- Lee H.-T., Takami M., Duan H.-Y., Karr J., Su Y.-N., Liu S.-Y., Froebrich D., Yeh C. C., 2012, *ApJS*, 200, 2
- López-Sepulcre A., Watanabe Y., Sakai N., Furuya R., Saruwatari O., Yamamoto S., 2016, *ApJ*, 822, 85
- Lucas P. W., et al., 2008, *MNRAS*, 391, 136
- Makin S. V., Froebrich D., 2018, *ApJS*, 234, 8
- Manoj P., et al., 2013, *ApJ*, 763, 83
- Manoj P., et al., 2016, *ApJ*, 831, 69
- Meyer D. M.-A., Vorobyov E. I., Kuiper R., Kley W., 2017, *MNRAS*, 464, L90
- Molinari S., et al., 2010, *A&A*, 518, L100
- Noriega-Crespo A., et al., 2004, *ApJS*, 154, 352
- Palau A., et al., 2018, *ApJ*, 855, 24
- Panwar N., Chen W. P., Pandey A. K., Samal M. R., Ogura K., Ojha D. K., Jose J., Bhatt B. C., 2014, *MNRAS*, 443, 1614
- Pezzuto S., et al., 2012, *A&A*, 547, A54
- Plunkett A. L., Arce H. G., Corder S. A., Mardones D., Sargent A. I., Schnee S. L., 2013, *ApJ*, 774, 22
- Povich M. S., Whitney B. A., 2010, *ApJ*, 714, L285
- Povich M. S., et al., 2007, *ApJ*, 660, 346
- Povich M. S., et al., 2009, *ApJ*, 696, 1278
- Povich M. S., et al., 2013, *ApJS*, 209, 31
- Povich M. S., Townsley L. K., Robitaille T. P., Broos P. S., Orbin W. T., King R. R., Naylor T., Whitney B. A., 2016, *ApJ*, 825, 125
- Raga A. C., Riera A., González-Gómez D. I., 2010, *A&A*, 517, A20
- Ragan S., et al., 2012, *A&A*, 547, A49
- Ramos-Larios G., Guerrero M. A., Sabin L., Santamaría E., 2017, *MNRAS*, 470, 3707
- Ray T. P., 2007, in Bouvier J., Appenzeller I., eds, IAU Symposium Vol. 243, Star-Disk Interaction in Young Stars. pp 183–194,
[doi:10.1017/S1743921307009544](https://doi.org/10.1017/S1743921307009544)
- Reach W. T., et al., 2006, *AJ*, 131, 1479
- Rebull L. M., et al., 2011, *ApJS*, 193, 25
- Reid M. A., Wilson C. D., 2006, *ApJ*, 644, 990
- Robitaille T. P., Whitney B. A., Indebetouw R., Wood K., Denzmore P., 2006, *ApJS*, 167, 256

- Robitaille T. P., Whitney B. A., Indebetouw R., Wood K., 2007, *ApJS*, **169**, 328
- Rosolowsky E., et al., 2010, *ApJS*, **188**, 123
- Ryabukhina O. L., Zinchenko I. I., Samal M. R., Zemlyanukha P. M., Ladeyschikov D. A., Sobolev A. M., Henkel C., Ojha D. K., 2018, preprint, ([arXiv:1802.08030](https://arxiv.org/abs/1802.08030))
- Sahai R., Claussen M., Sánchez Contreras C., Morris M., Sarkar G., 2008, *ApJ*, **680**, 483
- Sahai R., Lee C.-F., Sánchez Contreras C., Patel N., Morris M. R., Claussen M., 2017, *ApJ*, **850**, 158
- Samal M. R., Pandey A. K., Ojha D. K., Chauhan N., Jose J., Pandey B., 2012, *ApJ*, **755**, 20
- Samal M. R., et al., 2014, *A&A*, **566**, A122
- Samal M. R., et al., 2015, *A&A*, **581**, A5
- Stanke T., McCaughrean M. J., Zinnecker H., 2002, *A&A*, **392**, 239
- Stutz A. M., et al., 2013, *ApJ*, **767**, 36
- Tafalla M., Bachiller R., Lefloch B., Rodríguez-Fernández N., Codella C., López-Sepulcre A., Podio L., 2015, *A&A*, **573**, L2
- Takami M., Karr J. L., Koh H., Chen H.-H., Lee H.-T., 2010, *ApJ*, **720**, 155
- Takami M., Karr J. L., Nisini B., Ray T. P., 2011, *ApJ*, **743**, 193
- Takami M., Chen H.-H., Karr J. L., Lee H.-T., Lai S.-P., Minh Y.-C., 2012, *ApJ*, **748**, 8
- Tan J. C., Kong S., Zhang Y., Fontani F., Caselli P., Butler M. J., 2016, *ApJ*, **821**, L3
- Tang X. D., et al., 2017, *A&A*, **598**, A30
- Teixeira G. D. C., Kumar M. S. N., Bachiller R., Grave J. M. C., 2012, *A&A*, **543**, A51
- Thronson Jr. H. A., Lada C. J., 1983, *ApJ*, **269**, 175
- Traficante A., Fuller G. A., Smith R. J., Billot N., Duarte-Cabral A., Peretto N., Molinari S., Pineda J. E., 2018, *MNRAS*, **473**, 4975
- Umemoto T., et al., 2017, *PASJ*, **69**, 78
- Vázquez-Semadeni E., González-Samaniego A., Colín P., 2017, *MNRAS*, **467**, 1313
- Vorobyov E. I., Basu S., 2015, *ApJ*, **805**, 115
- Weingartner J. C., Draine B. T., 2001, *ApJ*, **548**, 296
- Whitney B. A., Wood K., Bjorkman J. E., Wolff M. J., 2003a, *ApJ*, **591**, 1049
- Whitney B. A., Wood K., Bjorkman J. E., Cohen M., 2003b, *ApJ*, **598**, 1079
- Williams J. P., Cieza L. A., 2011, *ARA&A*, **49**, 67
- Wilson T. L., Hanson M. M., Muders D., 2003, *ApJ*, **590**, 895
- Wu Y. W., et al., 2014, *A&A*, **566**, A17
- Zhang M., et al., 2013, *A&A*, **553**, A41
- Zhang M., Wang H., Henning T., 2014, *AJ*, **148**, 26
- Zhang M., Fang M., Wang H., Sun J., Wang M., Jiang Z., Anathipindika S., 2015, *ApJS*, **219**, 21
- Zinchenko I., et al., 2015, *ApJ*, **810**, 10
- Zinchenko I., Liu S.-Y., Su Y.-N., Wang Y., 2018, preprint, ([arXiv:1801.10331](https://arxiv.org/abs/1801.10331))

APPENDIX A: DETAILS OF THE CLASSIFICATION OF YOUNG STELLAR OBJECTS

Based on IRAC colours or fitting models to the observed SEDs or excess X-ray emission, a number of studies have been made in the literature to identify YSOs in the M17 complex (Povich et al. 2009; Povich & Whitney 2010; Povich et al. 2013; Broos et al. 2013; Bhavya et al. 2013, hereafter literature catalogues). For identifying potential YSO candidates in the vicinity of the jets/knots, we began our search by using the above literature catalogues, however, these catalogues are incom-

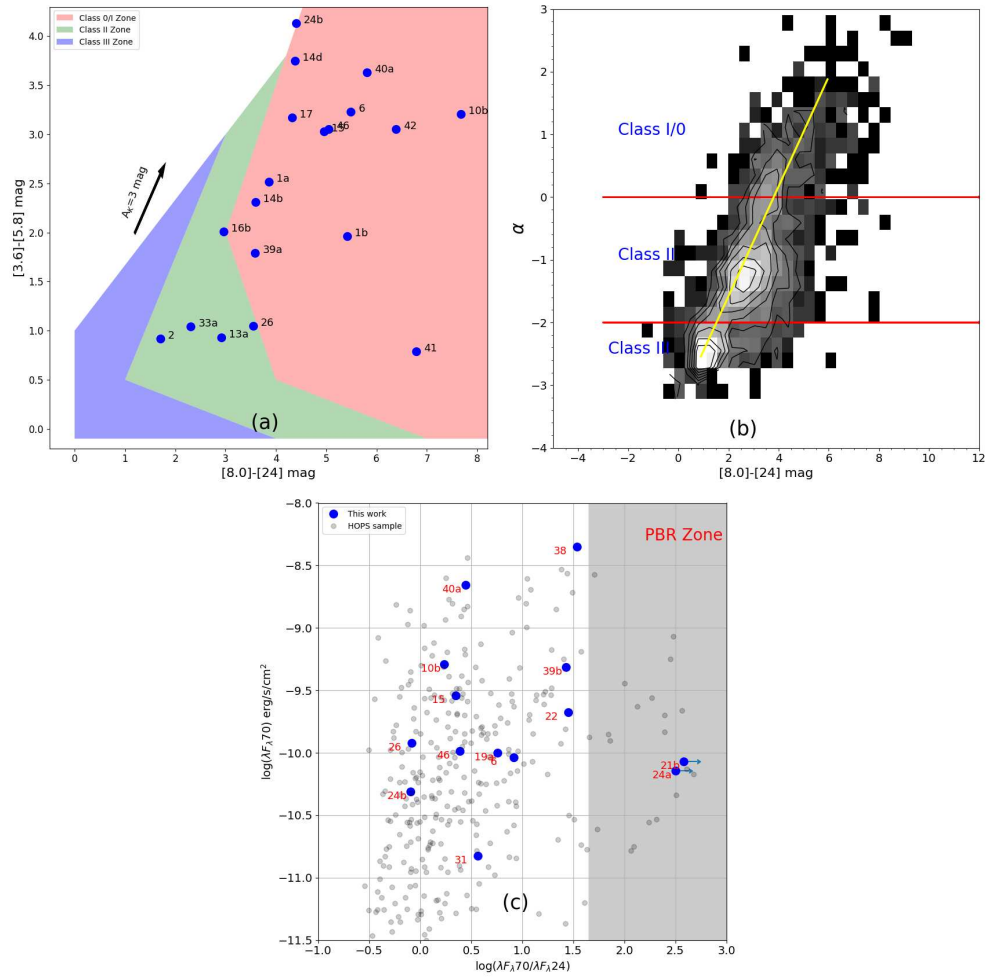


Figure A1. Classification of the potential driving sources with different criteria. (a): $[3.6] - [5.8]$ versus $[8.0] - [24]$ colour-colour plot of all the potential outflow driving sources (blue dots). (b): Hess diagram between $[8] - [24]$ colour and α of the [Dunham et al. \(2015\)](#)'s YSO sample. The yellow line corresponds to the linear fit to the peak of $[8] - [24]$ colour distribution, binned in α . (c): $70 \mu\text{m}$ flux versus $70 \mu\text{m}$ to $24 \mu\text{m}$ flux ratio for the potential outflow driving candidates (blue dots). Sources without $24 \mu\text{m}$ detection are indicated with arrow marks. The shaded area (i.e. $\log(\lambda F_{\lambda 70})/(\lambda F_{\lambda 24}) > 1.65$) represents the zone where early class 0 objects (or PBRs) lie. The protostars from the HOPS sample are shown in grey dots.

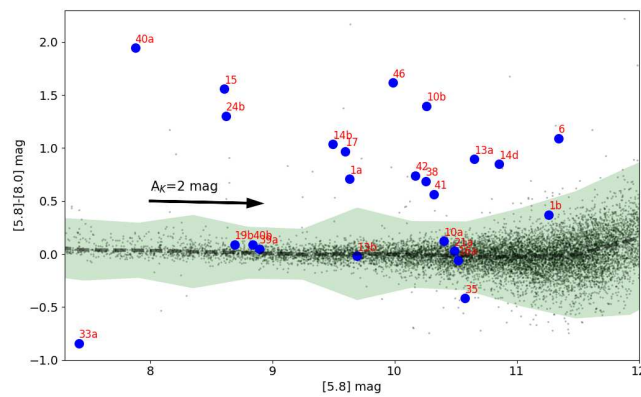


Figure A2. $[5.8] - [8.0]$ versus $[5.8]$ colour-magnitude diagram for the potential outflow driving candidates (blue dots) and sources of the field region (black dots). The shaded area represents the $\pm 3\sigma$ zone around the median $[5.8] - [8.0]$ colour of the field stars.

plete as none of them have incorporated the 70 μm data and some of them have not used 24 μm data. Moreover, we found many bright 24 μm sources in the vicinity of the jets/knots are either visible in only one or two IRAC bands (e.g. see Fig. 3). These sources could be YSOs, but not listed in the literature as they failed to pass through the colour combinations or data range used for the YSO identification. Since we are interested only in those sources that are close to the jets/knots and, moreover, the number of MHOs in our case is reasonably small, a detailed inspection and classification of point sources around each MHO are possible. Therefore, in addition to the above literature catalogues, we used a set of colour diagnosis between 3.6 to 70 μm (described below) to classify all those potential point sources (e.g. see sources 21a, 21b and 21c in Fig. 3) whose possibility as an outflow driving source exists. We particularly paid attention to those sources that are detected at 24/70 μm and lies close to the jets/knots. For sources that are visible at $\leq 8\mu\text{m}$, we mostly used literature catalogues to infer their evolutionary status.

The infrared spectral index (α), which is the slope of the SED between 2 and 24 μm , is used as an indicator of the YSO evolutionary stage (Lada 1987). In this scheme, α value > 0 represents class 0 or I classes (i.e. rising SED sources with strong spherical envelopes), α value between 0 to -2 represents class II class (i.e. PMS stars with optically thick accreting discs) and α value between -2 to -3 represents class III class (i.e. PMS stars with little or no discs left). Robitaille et al. (2006) introduced the alternative nomenclature “stage 0/I, II, III”, equivalent to the above classes, but based on the physical properties of the YSOs obtained using radiative transfer models. Based on the distribution of the young sources of the above classes or stages on the IRAC and MIPS colour-colour diagrams, several colour schemes have been developed in the literature to classify YSOs (e.g. Allen et al. 2004; Gutermuth et al. 2009; Robitaille et al. 2007; Rebull et al. 2011). However, we note that ambiguity is an inherent property of any YSO taxonomy, whether based upon colours, spectral indices or physical properties, and various schemes can alter classification by 20 to 30 per cent (e.g. Crapsi et al. 2008; Heiderman & Evans 2015; Carney et al. 2016). Keeping this caveat in mind, for simplicity, here we used the term “class” to refer either the physical stage or observational class of a YSO and adopt the following colour schemes to classify the potential sources into various YSO classes:

(i) For those potential sources that are detected in both the IRAC and MIPS bands, we used the [3.6] – [5.8] versus [8.0] – [24] colour-colour scheme (Robitaille et al. 2007) for classification. The distribution of such sources in the [3.6] – [5.8] versus [8.0] – [24] colour-colour space is shown in Fig. A1a. As can be seen, the majority of these sources are class 0/I-type YSOs. Though

34 *Samal et al.*

high extinction can affect the above classifications, the effect should be minimal in our case. For example, even if we deredden the sources with a foreground extinction of $A_K \sim 3$ mag (indicated in the figure), most of our candidates will still remain in the zone of class 0/I.

(ii) We observed that a few potential point sources in the vicinity of jets/knots are invisible at $3.6 \mu\text{m}$ or $4.5 \mu\text{m}$, yet are detected at $\geq 5.8 \mu\text{m}$ (possibly due to extreme visual extinction), while a few other point sources have no detection at 5.8 and/or $8.0 \mu\text{m}$ band (likely due to low sensitivity of these bands) but are detected at $\geq 24 \mu\text{m}$. To classify the sources of the former category, we looked for a correlation between $[8] - [24]$ colour and α using the [Dunham et al. \(2015\)](#)'s YSO sample (shown in Fig. A1b). [Dunham et al. \(2015\)](#) compiled spectral energy distributions for 2966 YSOs and tabulate the infrared spectral index, bolometric luminosity, and bolometric temperature for each YSOs. As can be seen from Fig. A1b, despite a significant scatter, a strong correlation between $[8] - [24]$ colour and α is clearly evident in the figure. From this correlation, we infer that sources with $[8.0] - [24] \text{ mag} > 3.9$ and $3.9 > [8.0] - [24] \text{ mag} < 1.8$ are respectively, the class 0/I and class II spectral sources. To classify the sources of the latter category, following [Gutermuth et al. \(2009\)](#) suggestion, we considered them as class 0/I YSOs, if they have $[X] - [24] \text{ colour} > 4.5$ mag, where $[X]$ is the photometry in any of the first two IRAC bands.

(iii) We also observed that in the vicinity of a few MHOs, some of the point sources are either invisible or very faint in $24 \mu\text{m}$ but significantly bright in $70 \mu\text{m}$ (e.g. the source 21b in Fig. 3). They could be deeply embedded YSOs of the complex. In such cases, we used the 24 and $70 \mu\text{m}$ color combinations for classification. The advantage of using $70 \mu\text{m}$ is that it is least sensitive to circumstellar extinction and geometry of the disc ([Dunham et al. 2006](#)) and proven as an important wavelength to identify early class 0 sources. For example, based on *Herschel* $70 \mu\text{m}$ observations, [Stutz et al. \(2013\)](#) identified 18 sources in the Orion complex that are visible at $\geq 70 \mu\text{m}$. They named these sources 'PACS Bright Red sources (PBRs)'. Comparing the SEDs of the PBRs with the radiative transfer models they infer that PBRs are very early class 0 objects, when the envelope is massive and the protostar still has to accrete most of its mass. They found that PBRs have very red mid- to far-infrared colours, i.e. $\log(\lambda F_\lambda 70)/(\lambda F_\lambda 24) \geq 1.65$. Their analysis also showed that the well-known class 0/I sources of the Orion complex from the *Herschel* Orion Protostar Survey (HOPS) have $\log(\lambda F_\lambda 70)/(\lambda F_\lambda 24) > 0.0$. We followed [Stutz et al. \(2013\)](#) criteria (shown in Fig. A1c) to understand the evolutionary status of the bright $70 \mu\text{m}$ sources as well as to confirm the classification of the YSOs (i.e. those sources with $70 \mu\text{m}$ detection) identified in the aforementioned schemes. As can be seen from Fig. A1c, most of the $70 \mu\text{m}$ detected sources (blue dots in the figure) have $\log(\lambda F_\lambda 70)/(\lambda F_\lambda 24)$ value greater than 0.0, therefore they are most likely

protostars. Among which, three sources are likely PBRs (one PBR is not shown in the plot owing to its high $\log(\lambda F_{\lambda 70})/(\lambda F_{\lambda 24})$ value).

(iv) For a few MHOs, we observed bright IRAC sources at the centre of bipolar flows with no 24/70 μm counterparts (e.g. the source 21a in Fig. 3). These sources could be low-luminosity class II/III YSOs, so the possibility of missing such YSOs in the aforementioned schemes exists. In such cases, we used literature catalogues, as many of them have used near-infrared and X-ray excess emission characteristics of the point sources to classify them as YSOs. It is worth mentioning that X-ray emission is more sensitive to the detection of class III YSOs while near-infrared excess is more sensitive to the detection of class II YSOs. In addition, we also used [5.8] versus [5.8] – [8.0] colour magnitude diagram (CMD) to examine the possibility of such sources as YSOs, because [5.8] – [8.0] colour is an extinction-free indicator as extinction laws are nearly same at 5.8 and 8.0 μm (e.g. $A_{5.8}/A_K=0.40$ and $A_{8.0}/A_K=0.41$; Weingartner & Draine (2001), see also Chapman et al. (2009)). Thus in the [5.8] versus [5.8] – [8.0] diagram, infrared-excess sources are expected to appear red in colour, whereas the background reddened sources in the direction of M17 would appear nearly colourless and are likely to fall in the zone of field stars. To see the distribution of field stars in the CMD, we used a field region located ~ 1 degree south-east of the H II region, and is devoid of cold dust emission and has no active site of star-formation as per SIMBAD database. Figure A2 shows the distribution of the field stars (grey dots) and all the potential IRAC sources including those already identified as YSOs in the aforementioned schemes (blue dots). From Fig A2, we considered a potential IRAC only source as a possible YSO, if its [5.8] – [8.0] colour is redder than 3σ of the median [5.8] – [8.0] colour of the field stars (shown as blue shaded area) at its corresponding 5.8 μm magnitude. Doing so, we found most of the potential IRAC only sources are likely field stars as most of them are located in the shaded area of the plot and none of them have been identified as YSOs in the literature.

In all the figures, the ID numbers represent the IDs assigned to the MHOs (see Table. 1), and the subscripts a, b and c, of a given ID represent the multiple potential sources of that ID that are under discussion (e.g. see Fig. 3). All the above potential driving sources are marked and discussed in Appendix B, where images of individual MHOs are shown and discussed.

After classifying all the potential sources into various YSO classes as described above, along with the catalogues of clumps/cores and other indicators, we looked for the most probable driving sources of the MHOs. The summary of our approach is briefly mentioned in Section 4.1 and the details are discussed in Appendix B when the individual MHOs are discussed. Briefly, we disqualified 12 nearby sources (these are IDs 1b, 2, 10a, 13b, 16a, 16b, 19b, 21a, 33a, 35, 39a and

36 *Samal et al.*

40b of Figs. A1 and A2) from our driving source list. Among the rest of the potential sources, we conclude 18 outflows are driven by protostars (class 0/I YSOs), 2 are driven by evolved sources (class II YSOs) and 4 are driven by one of the member of a group of YSOs (or small cluster).

APPENDIX B: MULTIWAVELENGTH IMAGES AND NOTES ON INDIVIDUAL MHOS

Here, we present multiwavelength figures around the MHOs and discussion concerning their morphologies, possible driving sources and association with dust the continuum clumps/cores, dark-clouds and SiO emission. In all the figures, the images and symbols, respectively, have the same meaning as in Fig. 3 and Fig. 4, except the SCUBA cores which are (if found) shown in diamond symbols. The figures and related discussion are available as supporting information with the online version of the article. We note that the reduced continuum subtracted H₂ images used in this work are publicly available at <http://astro.kent.ac.uk/uwish2/index.html>. And all the multiwavelength figures of the MHOs are available at the MHO database hosted at <http://astro.kent.ac.uk/df/MHCat/>.

APPENDIX B

Here, we present multiwavelength picture around the MHOs and discussion concerning their morphologies, driving sources and association with dust the continuum clumps/cores, dark-clouds and SiO emission. In all the figures, the images and symbols, respectively, have the same meaning as in Fig. 2 and Fig. 3 of the main draft, except the SCUBA cores which are (if found) shown in diamond symbols. In the figures, the arrows point to the possible potential driving sources that are under discussion.

- MHO 2308: This MHO constitutes two opposite elongated jets, forming a north-south flow (Fig. 1). Two $24\ \mu\text{m}$ point sources (labelled as 1a and 1b in the figure), separated by ~ 7.8 arcsec, were found between the jets. Both sources have the characteristics of a class 0/I YSO (see IDs 1a and 1b in Figs. A1a). Among the two, compared to 1b the source 1a lies exactly on the flow axis. We thus favour 1a as the responsible candidate for MHO 2308. Both sources are unresolved at $70\ \mu\text{m}$.
- MHO 2309: This MHO constitutes three compact knots connected with each other by some faint H_2 nebulosity. They appear to form a northeast-southwest outflow (Fig. 2). Along the likely flow axis, lies a bright IRAC source whose colors are characteristics of a field star (e.g. $5.8]=6.00$ mag and $[5.8] - [8.0]=0.22$; not shown in Fig. A2) and moreover the source is offset from the flow axis. We

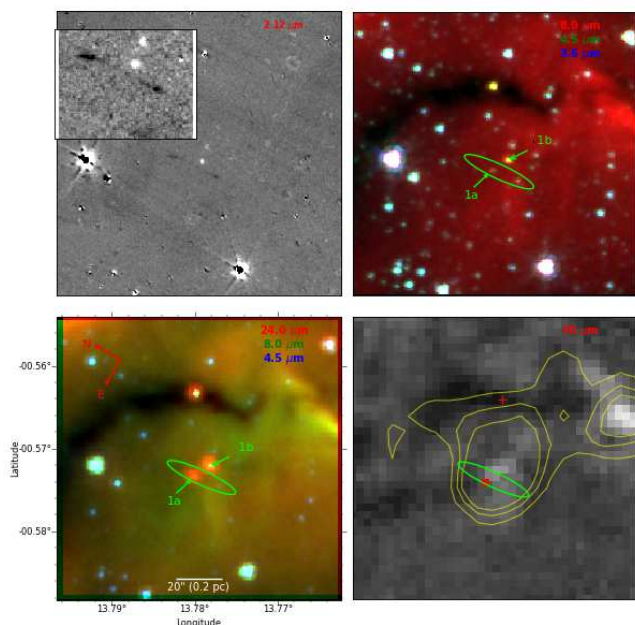


FIG. 1: Region of MHO 2308. The images and symbols, respectively, have the same meaning as in Fig. 2 and Fig.3 of the main text.

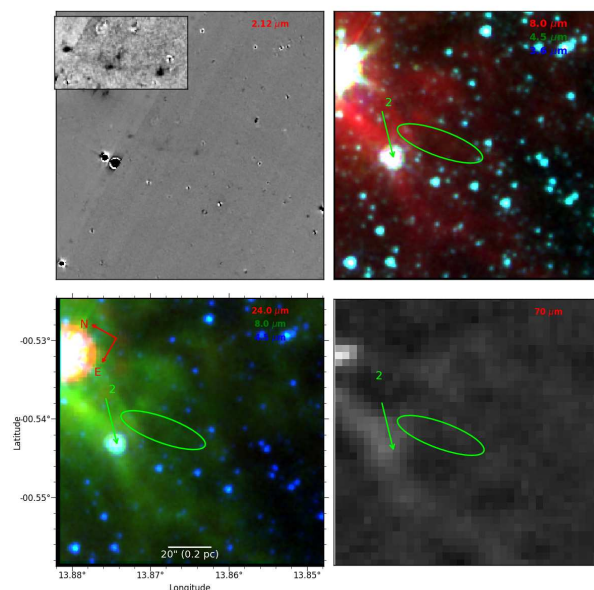


FIG. 2: Region of MHO 2309

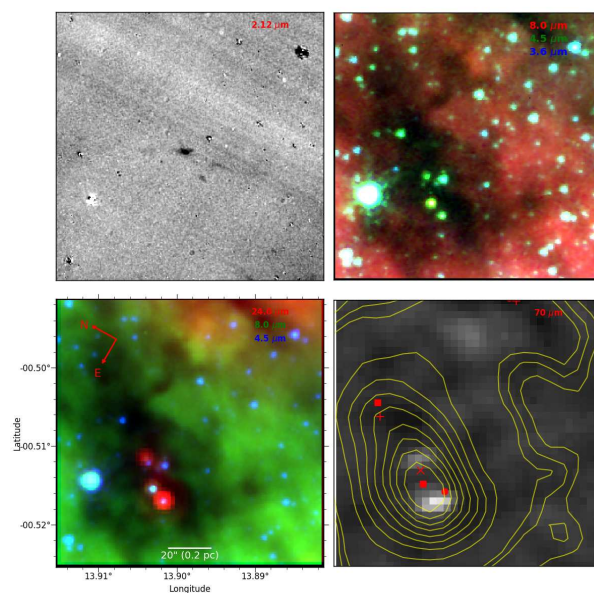


FIG. 3: Region of MHO 2310

therefore did not assign any driving source to MHO 2309.

- MHO 2310: This MHO consists of three H_2 emission features (Fig. 3). They are located at the outskirts of an elongated ATLASGAL clump. The clump is also the location of a SiO emission. Four $24\ \mu\text{m}$ point sources were found to be embedded in the clump. We suggest the jets/knots are driven by one or more members of this group or cluster.

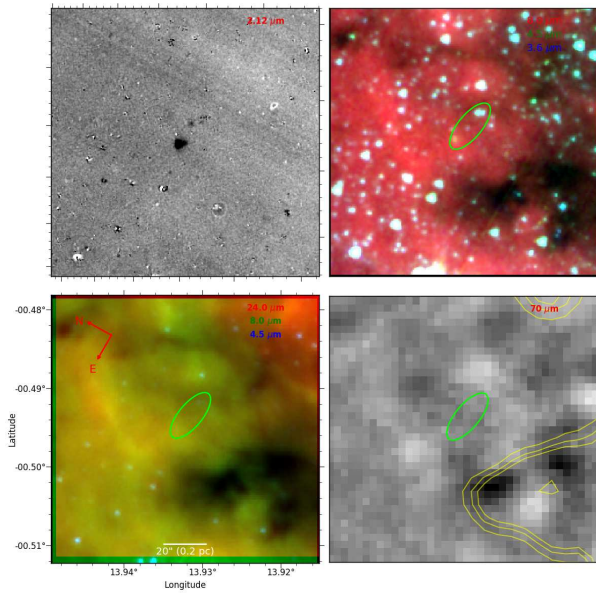


FIG. 4: Region of MHO 2311

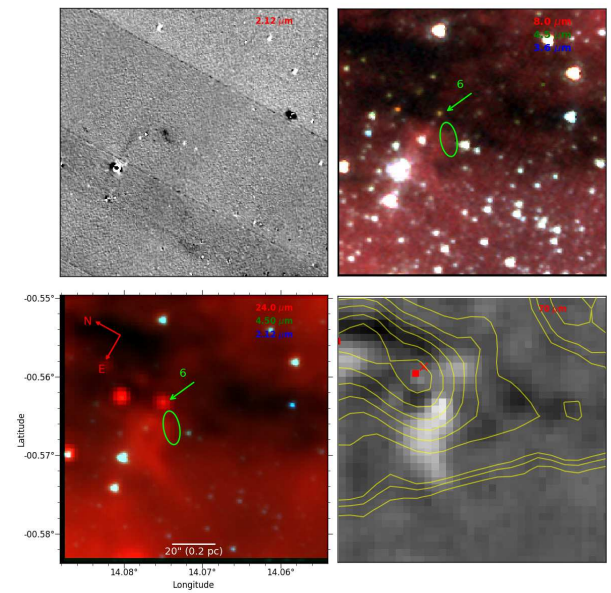


FIG. 6: Region of MHO 2313

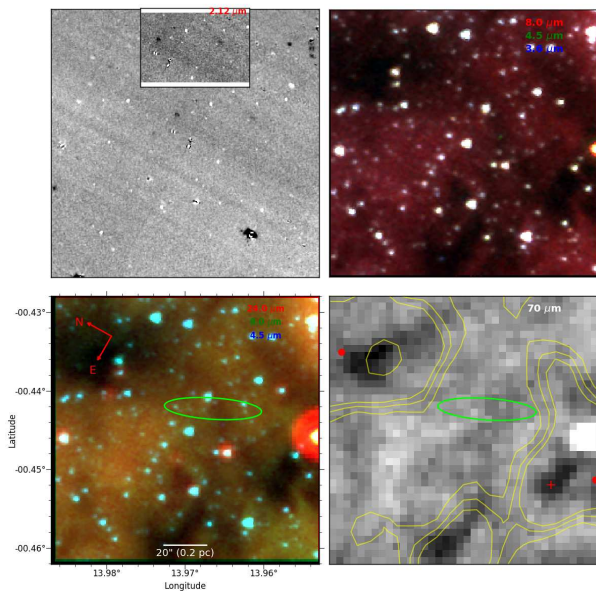


FIG. 5: Region of MHO 2312

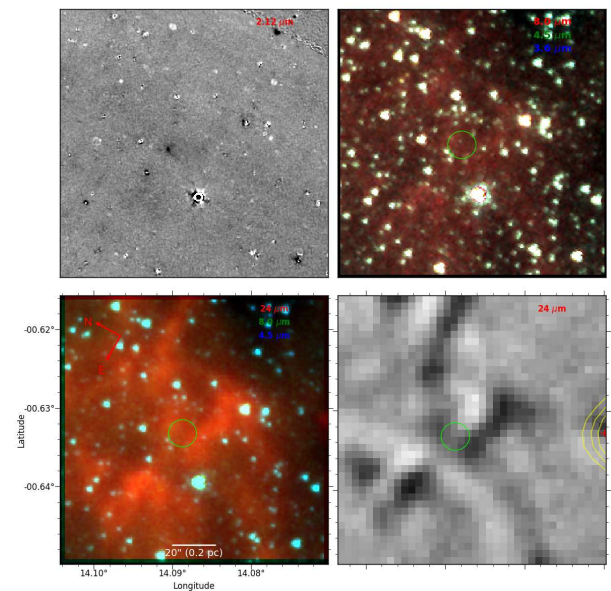


FIG. 7: Region of MHO 2314

- MHO 2311: This MHO constitutes two knots. Among the knots, the eastern knot is significantly brighter than the western knot (Fig. 4). No potential YSOs were found in the vicinity of this MHO.
- MHO 2312: This MHO constitutes two faint knot-like structures (Fig. 5). No potential YSOs were found along the presumed flow axis in the vicinity of the knots.
- MHO 2313: This MHO appears to be a patchy elongated emission feature (Fig. 6). At the base of the flow along the presumed flow axis, lies a 24 μm source (labelled as 6 in Fig. 6). The source has the

characteristics of a class 0/I YSO (see ID 6 in Figs. A1a and A1c) and at 70 μm it is relatively bright compared to other nearby sources. We thus favour the source 6 as the driving source of MHO 2313.

- MHO 2314: This MHO is a patch of emission with no YSOs or clumps in its vicinity (Fig. 7).

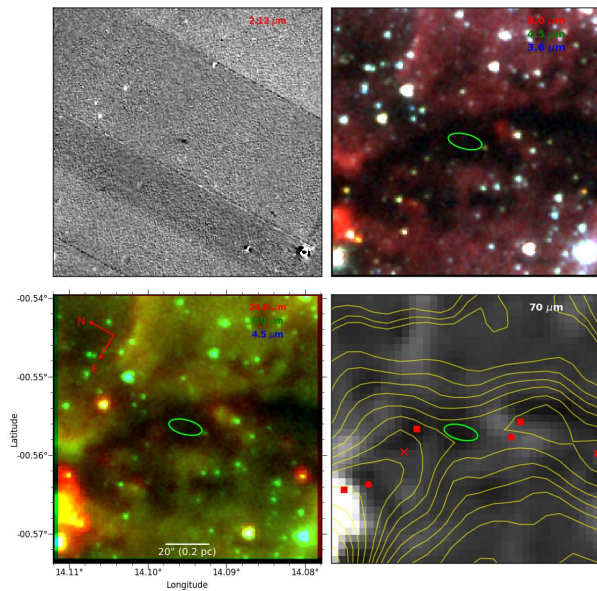


FIG. 8: Region of MHO 2315

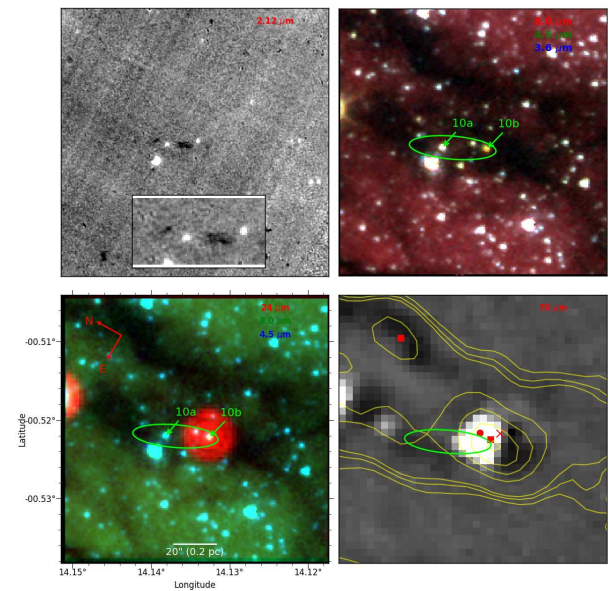


FIG. 10: Region of MHO 2317

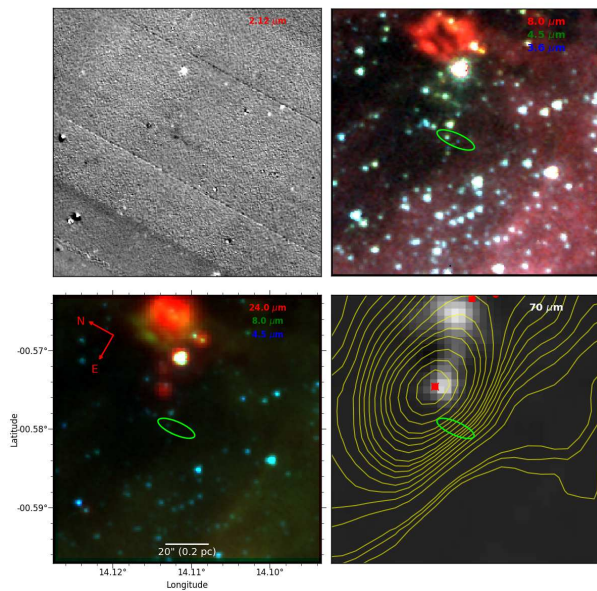


FIG. 9: Region of MHO 2316

- MHO 2315: This MHO appears to be a north-south oriented elongated emission structure (Fig. 8) and seems to be embedded in a *Spitzer* dark-cloud. No convincing 24/70 micron sources were found in its close vicinity. We thus did not assign any driving source to MHO 2315.
- MHO 2316: This MHO constitutes a few faint patchy emission features roughly oriented in north-south direction (Fig. 9). The emission features lie at the southeastern direction of an ATLASGAL clump. The clump is also the location of a SiO emission and is the host of a cluster of bright

IRAC/MIPS point sources. We suggest one of the cluster member is responsible for MHO 2316.

- MHO 2317: This MHO constitutes a bright elongated jet-like structure and two faint knots, forming a northeast-southwest oriented flow (see Fig. 10). Along the flow axis, a bright IRAC source is situated (labelled as 10a in the figure), however, the source is unlikely to be the driving source as its colours are more consistent with a field star (e.g. see ID 10a in Fig. A2) than a YSO. In the literature it is also not a YSO (e.g. Povich et al. 2010). On the other hand, at the southwestern end of the flow, lies a bright 24/70 μm source with colours (e.g. see ID 10b in Figs. A1a and A1c) characteristics of a class 0/I YSO. The source is embedded in an ATLASGAL clump and lies near to a SiO emission. We favour 10b as the driving source of MHO 2317.
- MHO 2318: This is an elongated knot with no apparent YSOs or clumps in its vicinity (Fig. 11).
- MHO 2319: This MHO consists of two bright knots and some patches of faint diffuse emission. They appear to form a northwest-southeast oriented flow (Fig. 12). Along the likely flow axis, although four bright IRAC sources can be seen, however, their IRAC colours (e.g. [5.8]-[8.0] colour) show characteristics of field stars (also they are not YSOs in the list of Povich et al. 2010). We therefore did not assign any driving source to MHO 2319.
- MHO 2320: This MHO is a weak diffuse emission feature in the vicinity of a bright field star (Fig. 13). Two bright IRAC point sources (marked as 13a and 13b) were found at the base of the flow in its north-eastern direction. Among the two, the

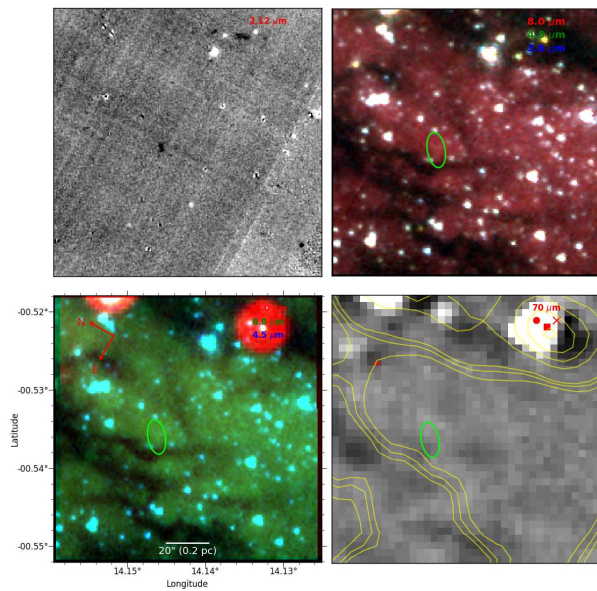


FIG. 11: Region of MHO 2318

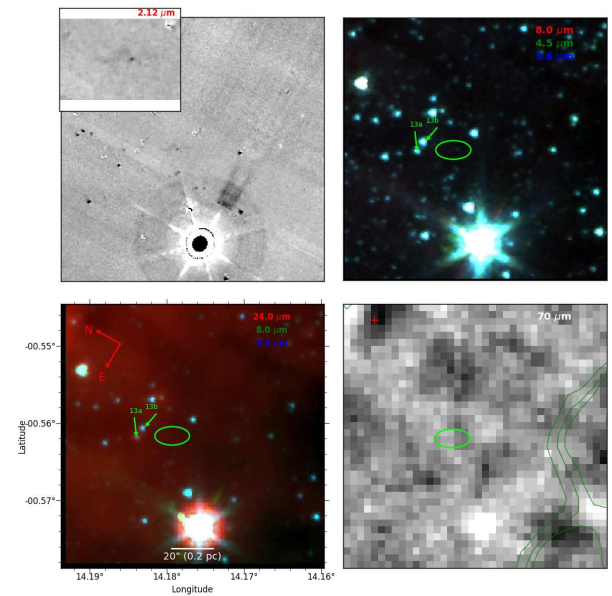


FIG. 13: Region of MHO 2320

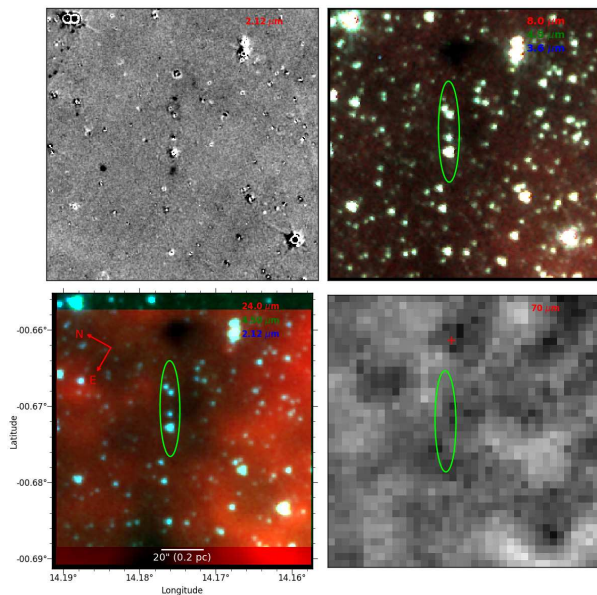


FIG. 12: Region of MHO 2319

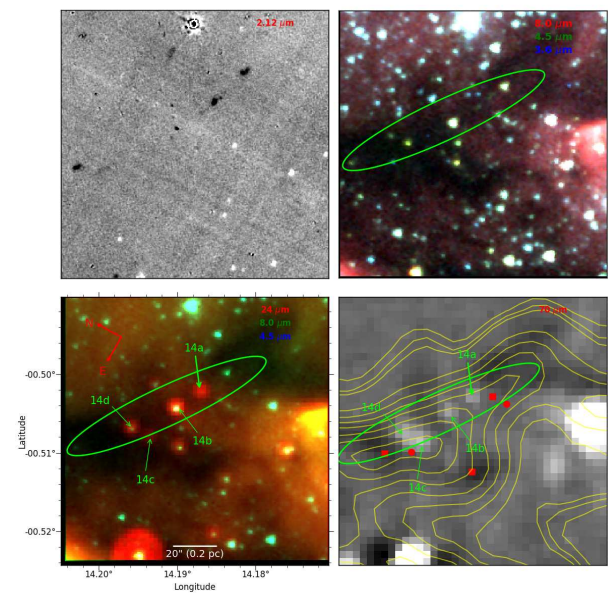


FIG. 14: Region of MHO 2321

source 13a is visible at $24 \mu\text{m}$ and has the characteristics (e.g. see ID 13a in Fig. A1a) of a class II YSO (see also Povich et al. 2010), while the source 13b is seen in only IRAC bands and appears to be a field star (see ID 13b in Fig. A2). We thus favour 13a as the possible potential driving source of MHO 2320.

- MHO 2321: This MHO constitutes three bright jet-like structures, aligned almost in a single line (Fig. 14). Along the flow line, we found four $24 \mu\text{m}$ sources (labelled as 14a, 14b, 14c and 14d). The source 14c is faint at $24 \mu\text{m}$ (no measurements in

the MIPS GAL catalogue), but relatively bright at $70 \mu\text{m}$, whereas 14a is invisible in IRAC last two bands but relatively bright in $24 \mu\text{m}$. We find the sources have colours (e.g. $[24]-[70]$ or $[8]-[24]$ or $[4.5]-[24]$) characteristic of a class 0/I YSOs. We suggest the driving source could be one member of this group of YSOs.

- MHO 2322: This MHO constitutes two compact knots. They appear to form a northeast-southwest oriented flow (Fig. 15). Close to the southwestern knot, lies a $24 \mu\text{m}$ point source, with colours (see ID 15 in Figs. A1a and A1c) characteristic a class

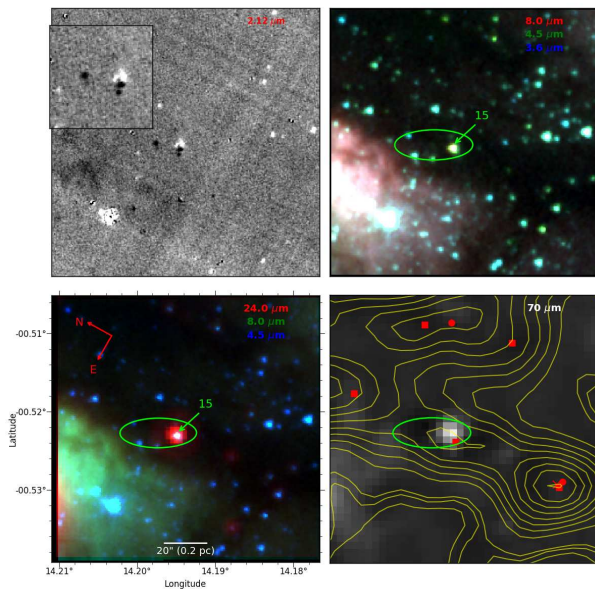


FIG. 15: Region of MHO 2322

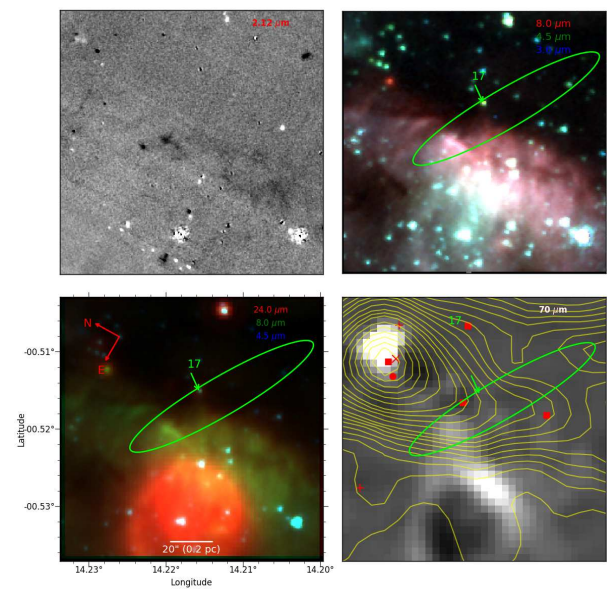


FIG. 17: Region of MHO 2324

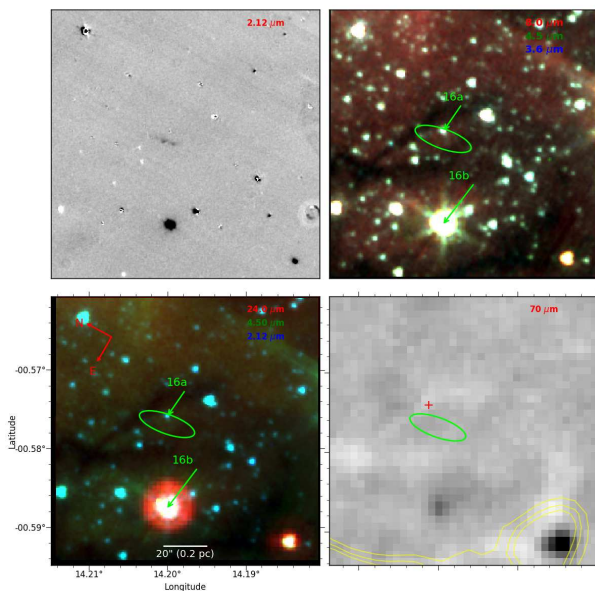


FIG. 16: Region of MHO 2323

0/I YSO, thus very likely the driving source of the flow.

- MHO 2323: This MHO consists of two faint knots (Fig. 16), connected with each other by some patchy H_2 nebosity. We do not find any potential YSO in its immediate vicinity. We note, the colours of the nearby bright IRAC source, 16a, has the properties of a non YSO (e.g. see Fig. A2), while though the nearby bright $24 \mu\text{m}$ source, 16b, has the colours characteristic of a class II YSO (e.g. $[8]-[24] = 2.98 \text{ mag}$; see ID 16b in Fig. A1a), however, this source cannot be effectively attributed

as the candidate responsible for MHO 2323. We therefore did not assign any driving source to MHO 2323.

- MHO 2324: This MHO constitutes of three aligned jet-like structures. They appear to form a southeast-northwest oriented flow (Fig. 17). Along the flow axis, between the knots, lies a faint $24 \mu\text{m}$ source (labelled as 17 in the figure) with colours (e.g. see ID 17 in Fig. A1a) characteristics of a class 0/I YSO. The source lies nearly middle of the flow and close to an ATLASGAL clump, making it as the likely potential candidate responsible for the flow.
- MHO 2325: This MHO has a head-tail morphology (see Fig. 18), suggesting the exciting source to be present in the tail direction, however, no YSOs/cores were found along the presumed flow direction.
- MHO 2326: This MHO constitutes a compact head and an elongated tail, and is associated to a $24 \mu\text{m}$ point source (Fig. 19). The source is quite faint in the IRAC bands but is relatively bright at 24 and $70 \mu\text{m}$ (labelled as 19a in Fig. 19). Its photometric colours (e.g. see ID 19a in Fig. A1c) are consistent with a class 0/I YSO. Thus the likely driving source of MHO 2326. We note, the IRAC colours of the nearby bright IRAC source, 19b, are not consistent with a YSO (e.g. see ID 19b in Fig. A2).
- MHO 2327: This MHO consists of three interconnected compact H_2 structures (Fig. 20). However, no YSOs or cores were found in its close vicinity.
- MHO 2328: This MHO corresponds to Fig. 3 of the

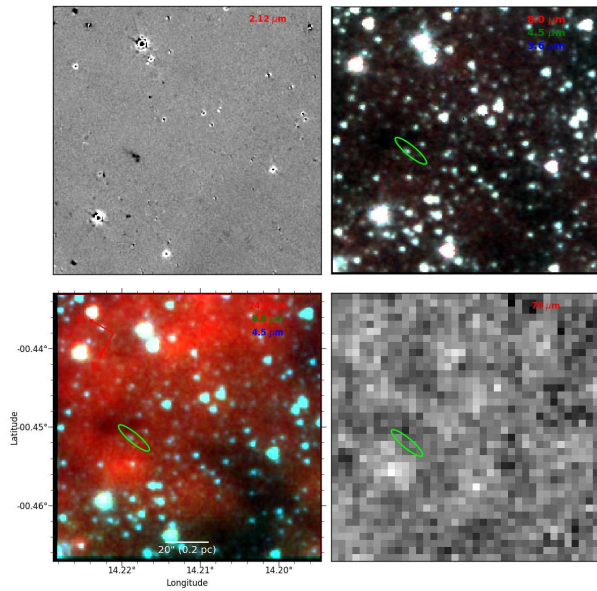


FIG. 18: Region of MHO 2325

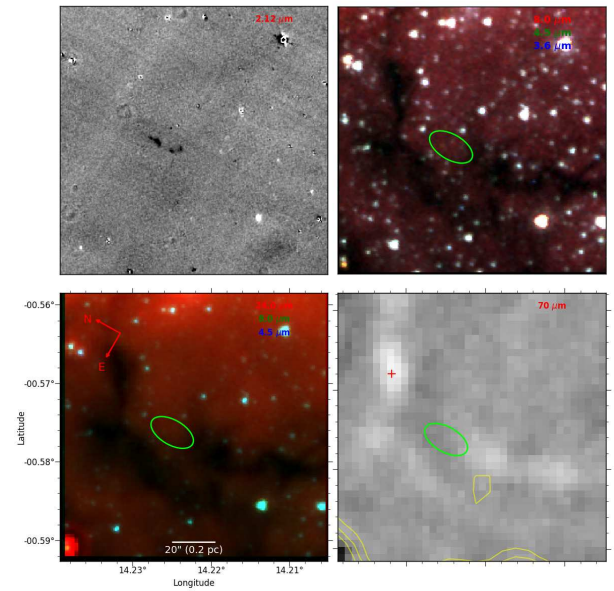


FIG. 20: Region of MHO 2327

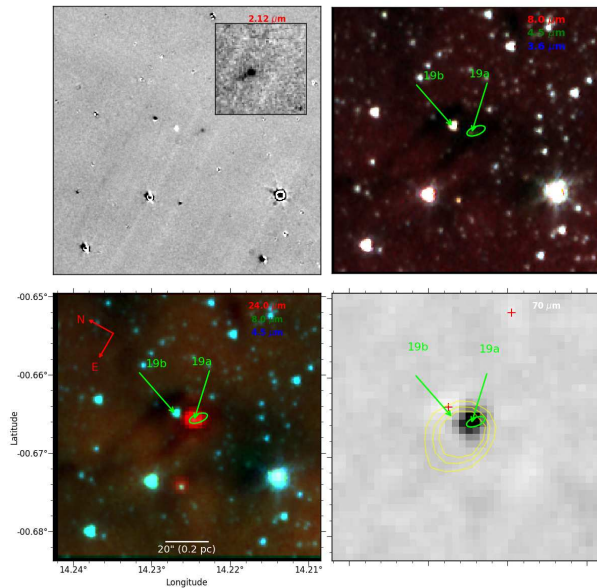


FIG. 19: Region of MHO 2326

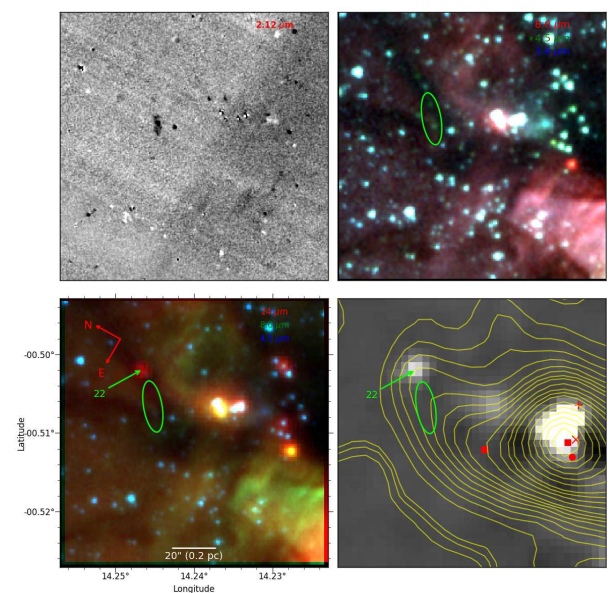


FIG. 21: Region of MHO 2329

paper, and is described in Section 4.1. It is driven by a PBR.

- MHO 2329: This is an elongated bow-shock shaped MHO (Fig. 21). Projecting back from the head of the bow-shock along the plausible jet axis, we found a $24 \mu\text{m}$ source (labelled as 22 in the figure) whose colours (e.g. see ID 22 in Fig. A1c) are consistent with a class 0/I YSO. We thus favour the source 22 as driving source of MHO 2329.
- MHO 2330: This MHO constitutes two compact knots and a faint bow-shock shaped structure. All together they appear as a northeast-southwest ori-

ented flow. No convincing YSOs or cores were found along the likely flow axis (Fig. 22).

- MHO 2331: This MHO constitutes several patches of H_2 emission. All together they appear as a northeast-southwest oriented flow (Fig. 23). Two sources were found at the southwestern end of the flow (labelled as 24a and 24b in the figure). Among the two, 24a is only visible in $70 \mu\text{m}$, and is located in the middle and western knots, while 24b is visible in all the bands between 3.6 to $70 \mu\text{m}$. 24a shows the characteristics of an early class 0 source or PBR (e.g. see ID 24a in Fig. A1c), while 24b is

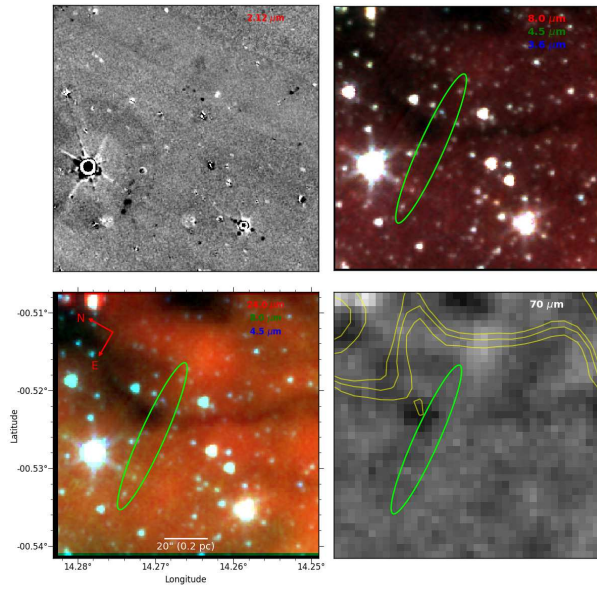


FIG. 22: Region of MHO 2330

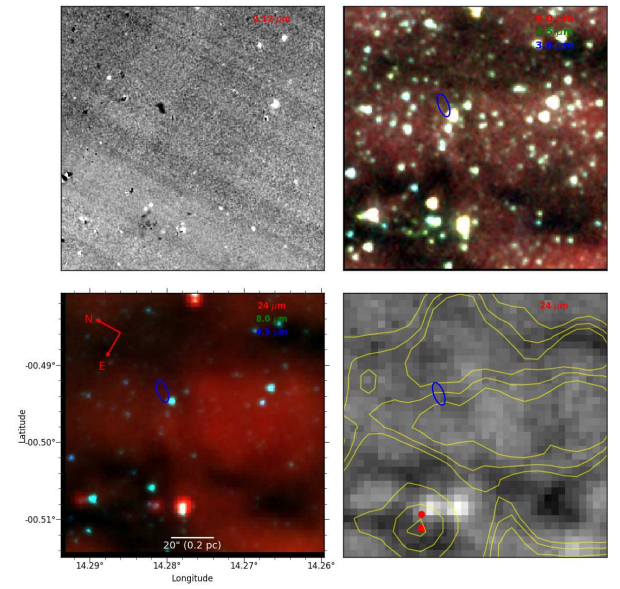


FIG. 24: Region of MHO 2332

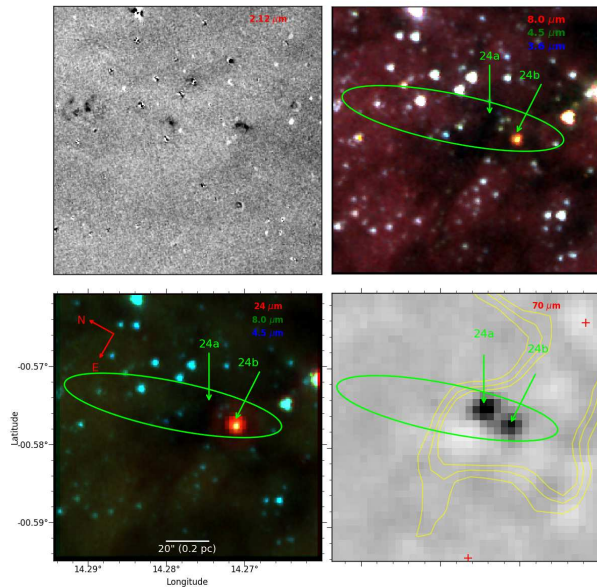


FIG. 23: Region of MHO 2331

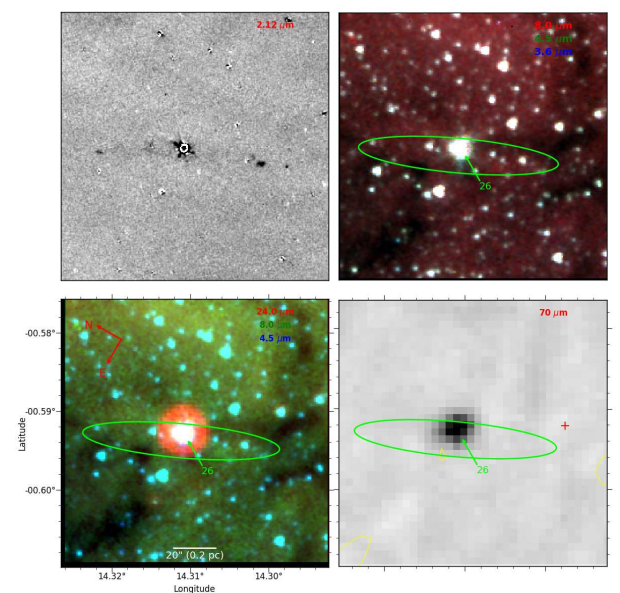


FIG. 25: Region of MHO 2333

likely a class II YSO (e.g. see also ID 24b in Fig. A1a). Either of them can be the driving source of the flow. Considering that the source 24a shows signs of an earlier evolutionary stage and luminous (i.e. bright at $70 \mu\text{m}$) compared to 24b, we favour the source 24a as the likely driving source of the flow, but we do not rule out the possibility of 24b as the driving source.

- MHO 2332: This MHO appears as a bright isolated knot in the H_2 image (Fig. 24) with no apparent YSOs or cores in its immediate vicinity.
- MHO 2333: This MHO constitutes a series of

jets/knots connected by some faint nebosity. All together they delineate as a northeast-southwest oriented flow (see Fig. 25). At the centre of the flow, lies a bright $24 \mu\text{m}$ point source (labelled as 26 in the figure), whose photometric colours (e.g. see ID 26 on Figs A1a and A1c) are consistent with a class II YSO. Thus the likely driving source of the flow. The H_2 features show some degree of bent morphology with respect to the source.

- MHO 2334: This MHO constitutes a series of faint knots connected by some faint nebosity. All together they appear to form a north-south oriented

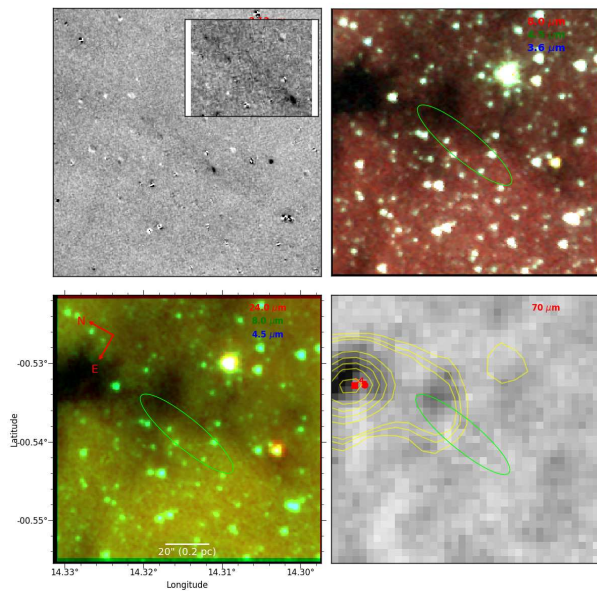


FIG. 26: Region of MHO 2334

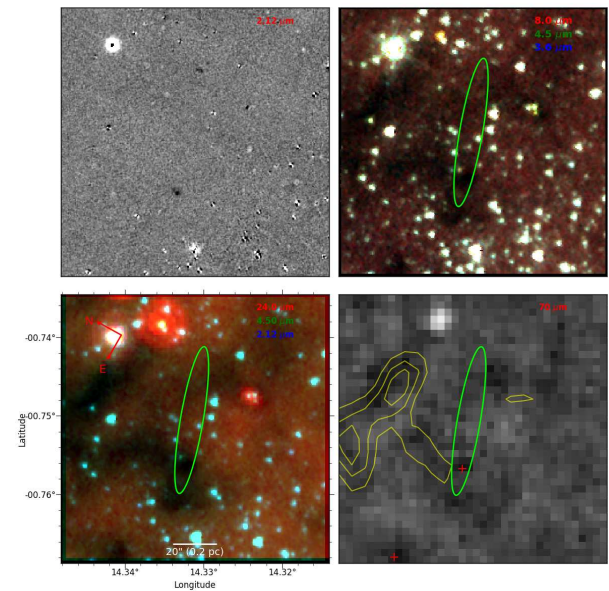


FIG. 28: Region of MHO 2336

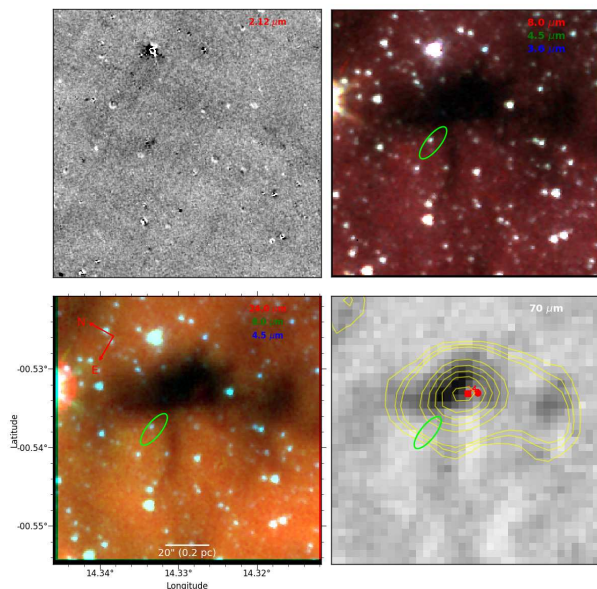


FIG. 27: Region of MHO 2335

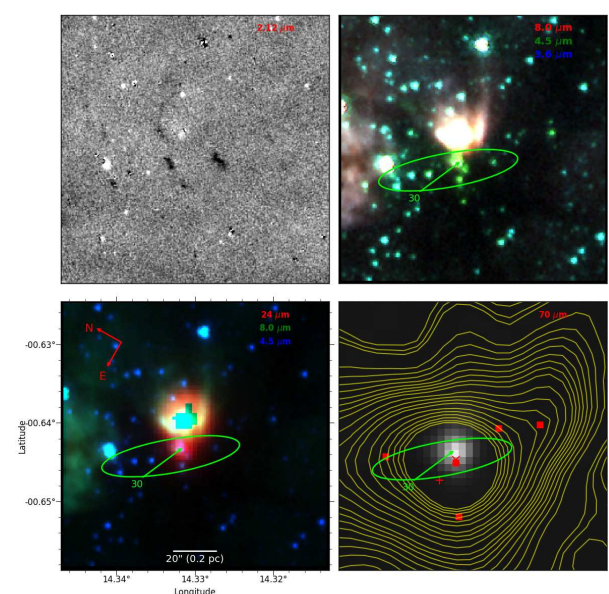


FIG. 29: Region of MHO 2306

flow (Fig. 26). No convincing potential 24/70 micron point sources or YSOs were found along the expected flow direction.

- MHO 2335: This MHO shows morphology of a east-west oriented flow. (Fig. 27). At the western end of the flow lies an ATLASGAL clump with no embedded 24/70 μm point sources. The clump is also the location of a SiO emission. We considered the clump as the likely origin of MHO 2335.
- MHO 2336: This MHO appears to be consists of two faint bow-shock like structures (Fig. 28). They appear to form a northwest-southeast oriented flow,

however, no convincing YSOs or cores were found along the presumed flow axis.

- MHO 2306: This MHO constitutes three emission features aligned roughly in a line. Together they delineate as a northeast-southwest flow, although molecular observation needed to see the actual connection of these features. This MHO is located at the southern direction of a diffuse infrared nebula (Fig. 29). The nebula is more prominent at 8 and 24 μm . This MHO is also site of an EGO, whose signature can be seen in the IRAC three-colour image as extended green emission. At the center of

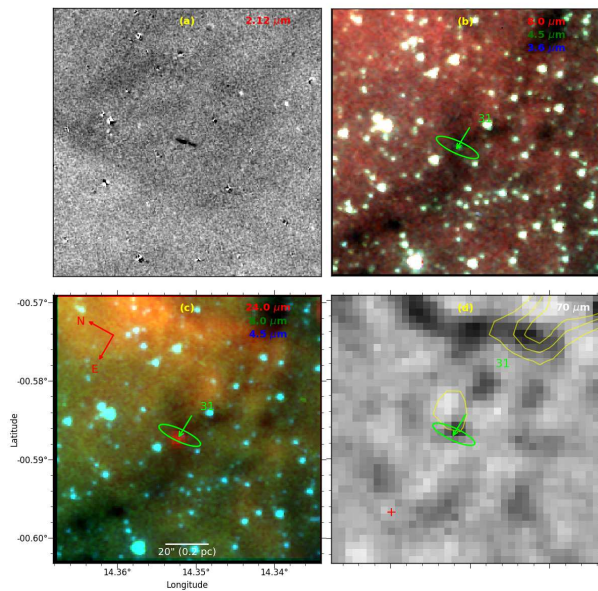


FIG. 30: Region of MHO 2337

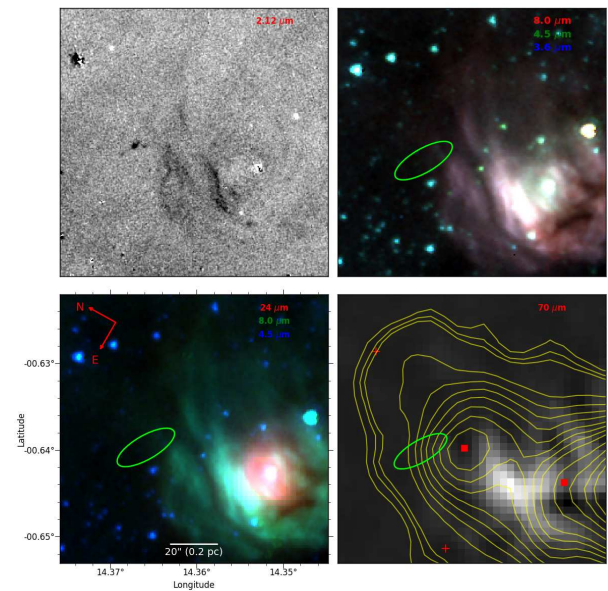


FIG. 31: Region of MHO 2338

the flow axis, lies a bright $70 \mu\text{m}$ source with a flux corresponds to a luminosity $\sim 5000 L_{\odot}$. The source has no counterpart in the MIPS GAL catalogue and it shows the characteristic of a PBR (not shown in Fig. A1c), indicating that the jet/knots are from an embedded luminous class-0 type massive YSO.

- MHO 2337: This MHO consists of two opposite jets (Fig. 30). They appear to emerge from a narrow filament. At the centre of the jets, along the flow axis, lies a $24 \mu\text{m}$ point source. The source has no *Spitzer*-IRAC counterparts, but its 24 to $70 \mu\text{m}$ flux ratio (e.g. see ID 31 in Fig. A1c) shows characteristics a class 0/I YSO. We favour the YSO as the driving source of the jets.
- MHO 2338: This region constitutes a bright compact knot (associated to a faint streamer) and many filamentary arc-like wispy structures (Fig. 31). The filamentary wispy structures lie in the vicinity of an infrared nebula. The nebula is quite prominent at 8.0 and $24 \mu\text{m}$. The orientations of the arc-like structures appear to be parallel to the $8 \mu\text{m}$ structures of the nebula, implying they are mostly from PDR. In contrast, the brightness and orientation of the compact knot and streamer pair are different from the thin filamentary structures, thus we considered the pair as an MHO. In the vicinity of the compact knot, no $24/70 \mu\text{m}$ point sources or YSOs were found. However, the presence of a compact dust continuum clump at the western end of the visible flow suggests that the clump is the likely origin of the flow.
- MHO 2339: This MHO shows an arc-like morphology in the H_2 image (Fig. 32). A bright $24 \mu\text{m}$

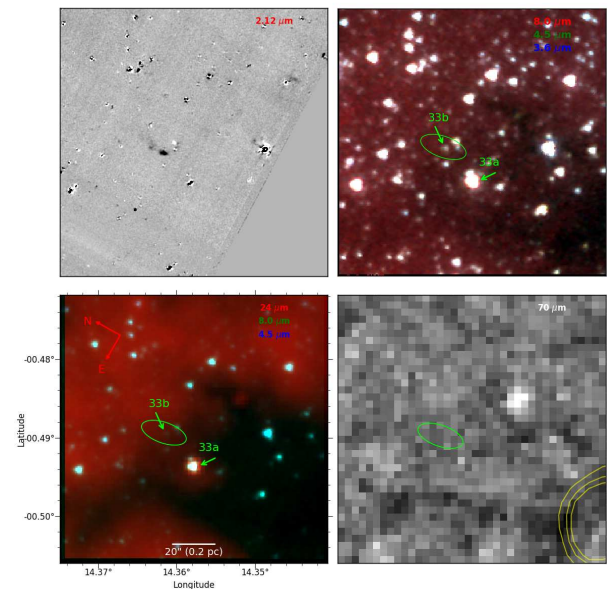


FIG. 32: Region of MHO 2339

source lies close to the MHO (labelled as 33a in Fig. 32), and its IRAC/MIPS colours (e.g. see ID 33a in Fig. A1a) are consistent with a class II YSO, but based on its $[5.8]-[8.0]$ color its class II status is bodacious. It cannot be effectively attributed as the driving source of MHO 2339 as it is not along the flow axis, moreover the concave side of the arc-like structure is not in the direction of 33a. No other YSOs or cores were found close to the source.

- MHO 2340: The morphology of this MHO suggests for a northwestern-southeastern oriented flow (see Fig. 33). We find no apparent driving source along

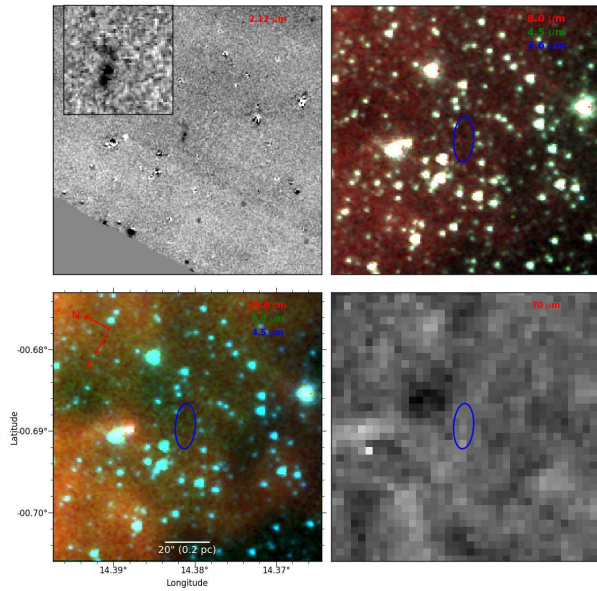


FIG. 33: Region of MHO 2340

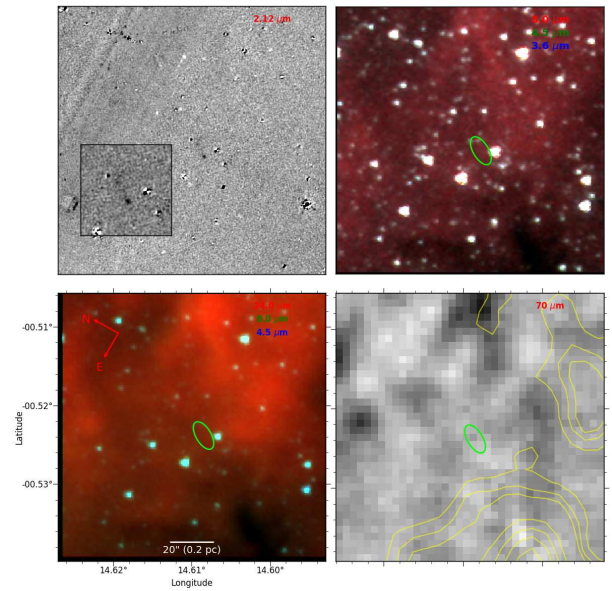


FIG. 35: Region of MHO 2342

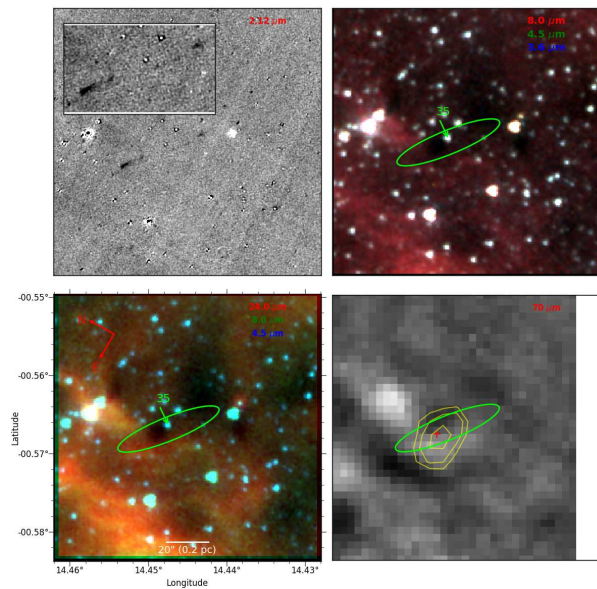


FIG. 34: Region of MHO 2341

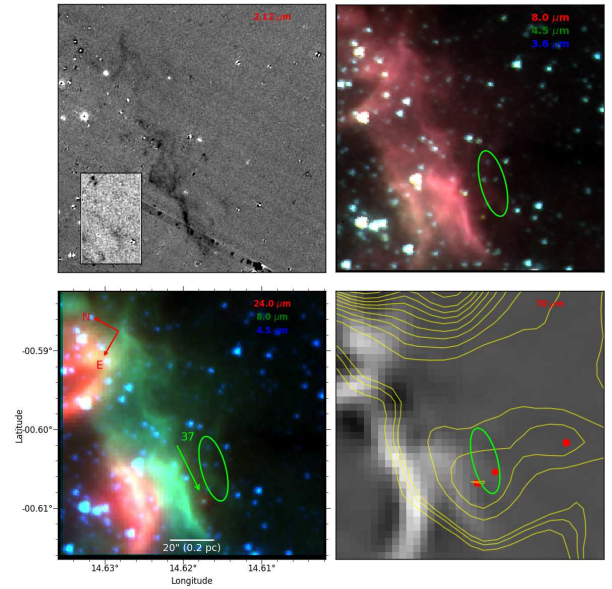


FIG. 36: Region of MHO 2343

the presumed flow axis of the MHO.

- MHO 2341: This MHO consists of two opposite elongated head-tail jet-like structures (Fig. 34). Together, they appear as an east-west bipolar flow. The morphology of the MHO suggests the probable driving source should be located between the jets. Although, we found an IRAC source (with no 24 μm counterpart) at the expected location (labelled as 35 in Fig. 34), but its colours match with that of field stars (e.g. $[5.8]-[8.0] = -0.41$; see ID 35 in Fig. A2), thus very unlikely to be the driving source. On the other hand, one can see a 870 μm clump close

to the centre of flow axis. We suggest the flow is likely originating from this core.

- MHO 2342: This MHO appears as a faint head-tail emission feature (Fig. 35). No potential YSOs/cores were found in its vicinity.
- MHO 2343: This MHO constitutes two compact knots and a faint wispy structure (Fig. 36), roughly appearing as a northwest-southeast oriented flow. It is located behind a PDR that is bright at 8.0 μm and 24 μm . At the southeastern end of the flow, lies a faint 24 μm source (labelled as 37 in Fig. 36), whose location coincides with the location of an

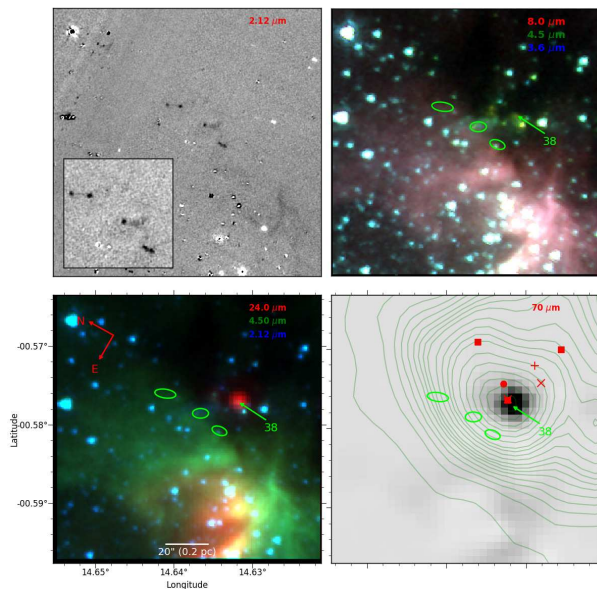


FIG. 37: Region of MHO 2344

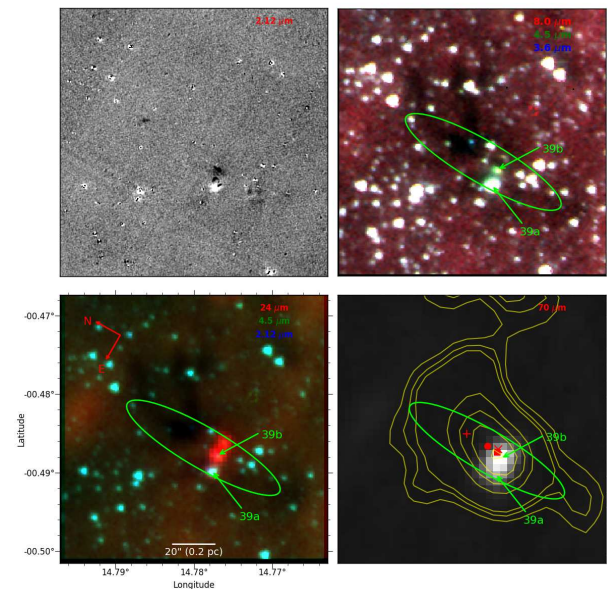


FIG. 38: Region of MHO 2345

ATLASGAL clump. The source has measurements only at 4.5 and 24 μm . Its $[4.5] - [24]$ colour ($= 8.5$ mag) suggests a class 0/I YSO. We favour the source 37 as the likely candidate responsible for the flow.

- MHO 2344: As can be seen from Fig. 37, this MHO constitutes three elongated H_2 features. They lie at the outskirts of an ATLASGAL clump. The clump also corresponds to the location of an EGO (G014.63-0.58), whose signature can also be seen in the IRAC three-colour image as diffuse extended green emission. At the centre of the clump, lies a 24/70 μm source, whose characteristics (e.g. $[8] - [24]$ or $[24] - [70]$ color; e.g. see ID 38 in Fig. A1c) are of a class 0/I YSO. The source is quite faint in the IRAC bands (e.g. not detected below 4.5 μm), indicates extinction is high in the direction of the clump. However, the source connects well to the middle jet though extended 4.5 μm emission, implying that the jet activity is most probably dominated by this source. High resolution molecular observation is needed to understand the nature of the multiple jets.
- MHO 2345: As evident from Fig. 38, this MHO constitutes several wispy emission features forming a north-south oriented outflow, with flow axis passing through two IRAC point sources (labelled as 39a and 39b in Fig. 38), located nearly at the middle of the flow. The source 39a has the characteristics of a non-YSO in IRAC colors (e.g. see ID 39a in Fig. A2) while it shows characteristics of a YSO in IRAC/MIPS diagram. The source 39b is not visible at 8.0 μm among the IRAC bands but appears to be bright at 24/70 μm with colours

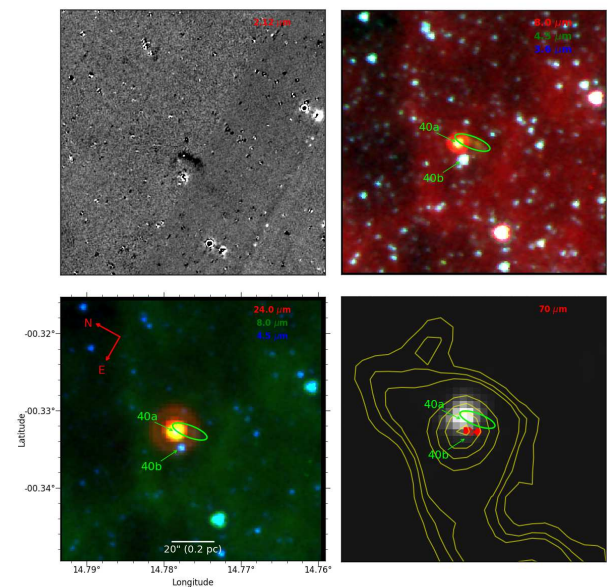


FIG. 39: Region of MHO 2346

(e.g. see also ID 39b in Fig. A1c) characteristics of a class 0/I YSO and is seems to be associated with some faint extended 4.5 μm emission. This source also lies close to a SiO emission. We favour 39b as the likely candidate responsible for this flow. We note, the 24/70 μm emission of this region seems to be elongated, possibly blended by the presence of a multiple sources, so the 24/70 μm magnitudes are probably not robust.

- MHO 2346: In H_2 , this MHO looks like an elongated east-west flow (Fig. 39). The flow is also visible at 4.5 μm . The MHO is embedded in an AT-

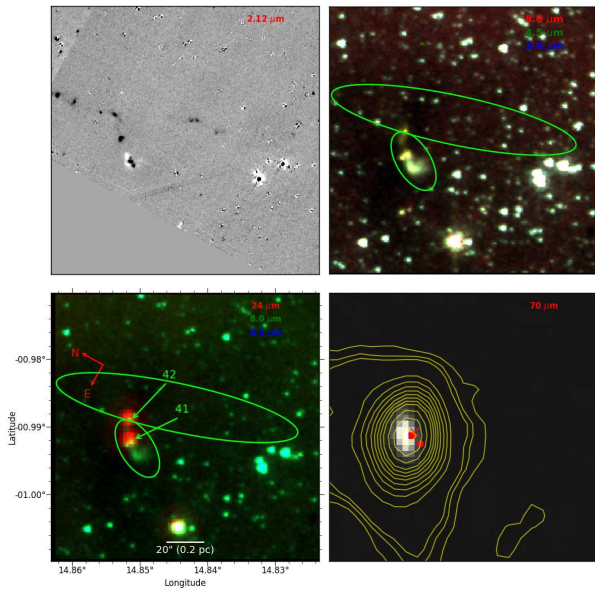


FIG. 40: Region of MHO 2347 and 2307.

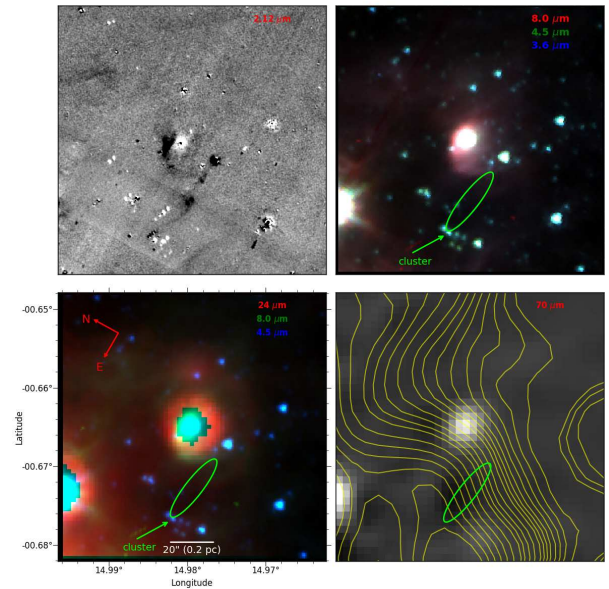


FIG. 41: Region of MHO 2348

LASGAL clump and also lies close to a SiO emission. At the base of the flow, lies a bright $24\ \mu\text{m}$ source (labelled as 40a in Fig. 39), with characteristics of a class 0/I YSO (e.g. see ID 40a in Fig. A1a and A1c), thus the likely driving source of the flow. We note, though a bright IRAC source (labelled as 40b in Fig. 39) lies close to the MHO, however, it is offset from the flow axis and its IRAC colours show characteristics of a non YSO (e.g. see ID 40b in Fig. A2).

- MHO 2347 and 2307: MHO 2347 contains a series of knots roughly oriented in northeast-southwest direction with some bend morphology (Fig. 40). A bright $24\ \mu\text{m}$ source (labelled as 42 in Fig. 40) lies slightly below the flow axis. Its photometric colours (see ID 42 in Fig. A1a) are consistent with a class 0/I YSO. Considering the bend morphology of the MHO, we favour 42 as the responsible candidate for the flow. We find the median spacing of the knots is about 0.16 pc. With this spacing and assuming a velocity of $\sim 35\ \text{km s}^{-1}$, we estimated the time between the knots to be about 5000 yr.

MHO 2307 constitutes bright extended nebulosity at $4.5\ \mu\text{m}$ and compact H_2 knots. Together they appear roughly as a northeast-southwest oriented flow. A $24\ \mu\text{m}$ point source (labelled as 41 in Fig. 40) lies between the flow with characteristics of a class 0/I YSO (see ID 41 in Fig. A1).

We note, both the above driving sources are unresolved at $70\ \mu\text{m}$.

- MHO 2348: As evident from Fig. 41, this MHO consists of two H_2 structures: (i) an arc-like structure around a bright star associated with a compact

H II region bright in $8\ \mu\text{m}$ and $24\ \mu\text{m}$, (ii) a bow-shock structure in the south-eastern direction of the bright star. In the first case, as the orientation of the arc-like structure appears to be parallel to the ionization front of the H II region, thus its origin is mostly from the PDR around the H II region. In the second case, as the head of bow-shock structure points in the north-western direction, the probable driving source is expected to be located in the south-eastern direction. No bright $24/70\ \mu\text{m}$ sources were found along the presumed direction. However, in the IRAC images, at the base of the bow-shock tail, a group of IRAC point sources can be seen. Some of them are YSOs (Povich et al. 2013). We suggest the driving source could be one of the members of this group or cluster.

- MHO 2349: This MHO shows an elongated morphology with a compact head and a diffuse tail (Fig. 42). We do not find any potential $24/70\ \mu\text{m}$ point sources or YSOs in the close vicinity of the MHO. However, the elongated tail, when traced backward points directly to an ATLASGAL clump, located in the northern direction of the MHO. The clump is also the location of a SiO emission, suggesting that a potential driving source could be embedded in the clump. However, since the clump is relatively far from the MHO, and we do not see any diffuse H_2 nebulosity connecting the core and the compact knot, we thus did not consider it as the responsible candidate of MHO 2349.
- MHO 2350: This MHO consists of two opposite jet-like structures. They appear to emerge from a narrow dark cloud, located at the middle of jets (Fig. 43). The absorption feature of the dark cloud

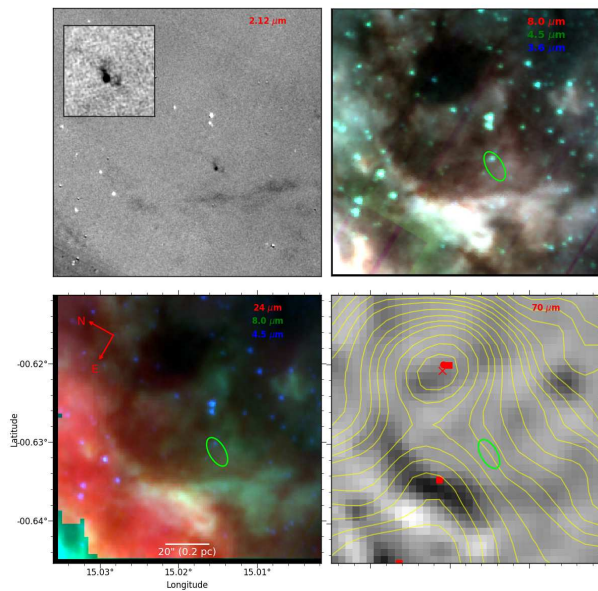


FIG. 42: Region of MHO 2349

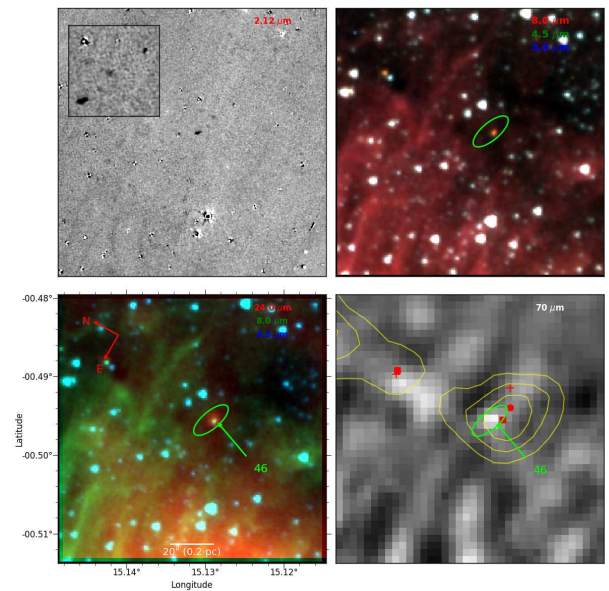


FIG. 44: Region of MHO 2351

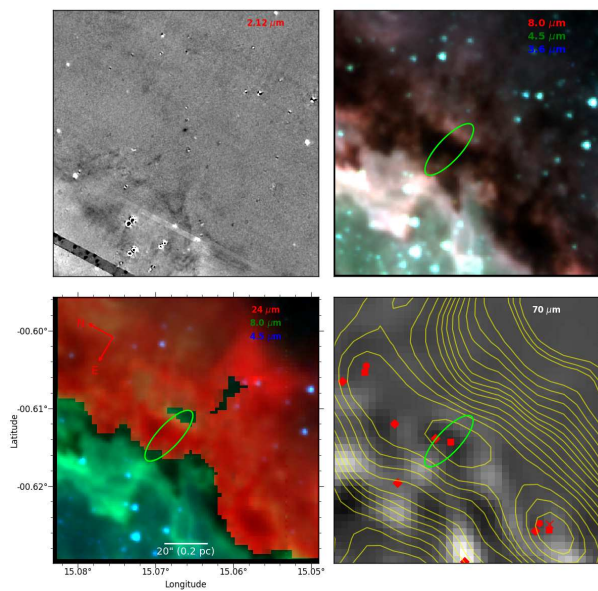


FIG. 43: Region of MHO 2350

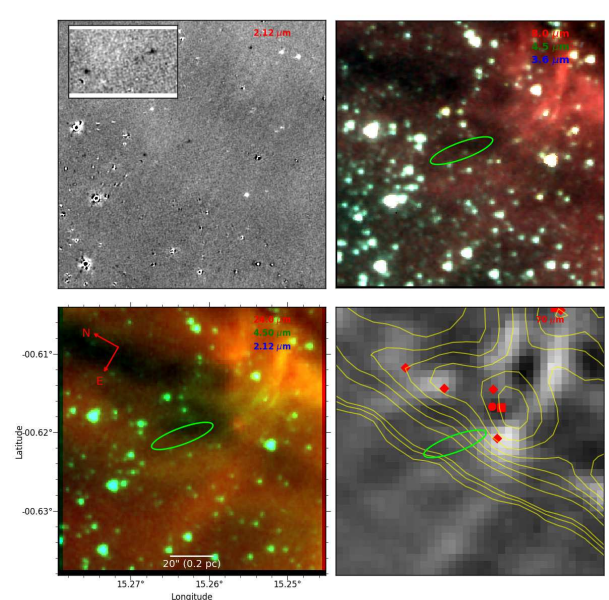


FIG. 45: Region of MHO 2353

against the bright background is more evident in the IRAC three-colour image. We do not find any point source between the jets. However, a SCUBA clump lies at the middle of the jets, indicating that the clump is the likely origin of the jets.

- MHO 2351: This MHO consists of three faint jets/knots (Fig. 44) aligned in a line. At the centre of the jets/knots, lies a $24 \mu\text{m}$ source (labelled as 46 in Fig. 44), whose photometric colours (e.g. see ID 46 in Figs. A1a and A1c) show characteristics of a class 0/I YSO. Thus the likely driving source of the MHO.

- MHO 2352: This MHO corresponds to Fig. 9, and is described in Section 5.1 of the paper. This MHO appears to be driven by a core.
- MHO 2353: This MHO appears to consist of two knot-like structures (see Fig. 45). Our search resulted in no potential YSOs along the flow axis. However, at one end of the flow, lies an ATLASGAL clump. We suggest the clump could be the origin of MHO 2353.